© 2018 Dongwei Fu

EXAMINATION OF THE BEHAVIOR OF MODIS-RETRIEVED CLOUD DROPLET EFFECTIVE RADIUS THROUGH MISR-MODIS DATA FUSION

BY

DONGWEI FU

THESIS

Submitted in partial fulfillment of the requirements
for the degree of Master of Science in Atmospheric Sciences
in the Graduate College of the
University of Illinois at Urbana-Champaign, 2018

Urbana, Illinois

Adviser:

Professor Larry Di Girolamo

ABSTRACT

Listed as one of the Essential Climate Variables by the Global Climate Observing System, the effective radius (*Re*) of the cloud drop size distribution plays an important role in the energy and water cycles of the Earth system. *Re* is retrieved from several passive sensors, such as the Moderate Resolution Imaging Spectroradiometer (MODIS), based on a visible and near-infrared bi-spectral technique that had its foundation more than a quarter century ago. This technique makes a wide range of assumptions, including 1-D radiative transfer, assumed single-mode drop size distribution, and cloud horizontal and vertical homogeneity. It is well known that deviations from these assumptions lead to bias in the retrieved *Re*.

Recently, an effort to characterize the bias in MODIS-retrieved *Re* through MISR-MODIS data fusion revealed biases in the zonal-mean values of MODIS-retrieved *Re* that varied from 2 to 11 μm, depending on latitude [Liang et al., 2015]. Here, in a push towards bias-correction of MODIS-retrieved *Re*, we further examine the bias with MISR-MODIS data fusion as it relates to other observed cloud properties, such as cloud horizontal heterogeneity, cloud optical depth, and sun-view geometry. Our results reveal that while *Re* bias do show a certain degree of dependence on some properties, no single property dominates the behavior in the MODIS-retrieved *Re* bias. Through data stratification by observed cloud properties and latitude, we introduce a bias-correction approach for MODIS-retrieved *Re* at regional scales. Our estimates reveal global distribution of MODIS-retrieved *Re* monthly mean bias ~1 to 12 μm depending on latitude and cloud types, the bias-corrected *Re* estimates of ~ 4 to 16 μm are consistent with available validations of MODIS *Re* reported in previous studies over limited regions. Removing the mean bias from the original MODIS $Re_{2.1}$ and $Re_{3.7}$ monthly means show more consistent behavior

among the two channels that range from 0 to +0.6 μm in the marine stratocumulus regions and -2 to 0 μm in the cumuliform cloud regions. This curious finding seems to suggest that the vertical distribution of drop sizes for marine stratocumulus clouds are very different from other types of marine liquid water clouds.

ACKNOWLEDGEMENTS

I would like to thank my advisor Prof. Larry Di Girolamo for his guidance and support throughout this research. I am grateful for his patience and scientific insights, and that I am deeply encouraged by his passion and enthusiasm for research. Whenever I felt lost in my research, his inspirations would guide me back on track. I would also like to thank Dr. Lusheng Liang and Dr. Guangyu Zhao for their help and assistance throughout this research work, and Jesse Loveridge for help on my writing. Furthermore, I would like to thank Prof. Robert Rauber for the helpful discussion on my research. Thanks also goes to my office mates, Ming, Lee, Arka, Puja, Remy, it has been my great pleasure to work in the friendly environment of the Di Girolamo Research Group.

I would also like to thank my parents for always being there for me. Most importantly, thanks to Zhuoqun (Cece), the partner that constantly provides the utmost strength to keep me focused on my research.

This work was supported under NASA contract NNX14AJ27G and NNX16AMO7A and the MISR project through the Jet Propulsion Laboratory of the California Institute of Technology. Partial computational support comes from the Blue Waters sustained-petascale computing project, which is supported by NSF (awards OCI-0725070 and ACI-1238993) and the State of Illinois, USA. All supports are gratefully acknowledged.

Dedicated to my parents for their support.

TABLE OF CONTENTS

CHAPTER 1: INTRODUCTION

1.1 Background

1.1.1 Clouds and Climate

Clouds, one of the major components of the Earth's atmosphere, cover ~70 percent of the Earth [Wylie et al., 2007]. Clouds play an important role in regulating Earth's radiative energy budget and water cycle. Clouds both reflect incoming shortwave solar radiation and absorb longwave terrestrial radiation, which modulates the Earth's radiation balance; at the same time, however, clouds themselves are also created by the warming and cooling of the atmosphere. Changes in clouds would greatly impact the radiative energy balance and water exchanges that determine the climate. According to the Intergovernmental Panel on Climate Change (IPCC) Report from 2007, cloud feedbacks remain the largest source of uncertainty in climate sensitivity estimates [Solomon et al., 2007]. In other words, the way clouds are represented in climate models greatly impact uncertainties in predicting future climates, thus it is crucial for us to understand the role of clouds in the Earth system's climate, and to accurately represent clouds in our climate models. In doing so, it requires precise information of cloud microphysical and macrophysical properties over a long period. Satellite monitoring of the Earth have the advantages of good global coverage and continuously monitoring record. Its retrievals can be used to validate cloud parameterization of climate models in order to improve their performance. Thus, it is crucial that our satellite retrievals of cloud properties are accurate and reliable.

1.1.2 Cloud Droplet Effective Radius (*Re*)

The cloud droplet effective radius (*Re*), listed as one of the Essential Climate Variables by the Global Climate Observing System, serves to be the main focus of this thesis. *Re* is a weighted mean of the size distribution of cloud droplets [Hansen, 1971] defined as:

$$r_e = \frac{\int_0^\infty \pi \cdot r^3 \cdot n(r)\, dr}{\int_0^\infty \pi \cdot r^2 \cdot n(r)\, dr} \tag{1.1}$$

where *n(r)* is the size distribution and *r* is the radius of a cloud droplet. *Re* plays an important role in the energy and water cycle of the Earth system [Twomey, 1991; Platnick and Twomey, 1994]. *Re* has a wide range of applications, such as to assess aerosol-cloud interactions [e.g., Menon et al., 2008], and to evaluate cloud parameterization in climate models [e.g., Slingo, 1988; Song et al., 2012]. For example, given in the following relationship:

$$\tau = \int_{z=0}^{h} \frac{3q_L}{2\rho_w r_e} dz \tag{1.2}$$

where q_L is the liquid water content, τ is the optical depth, and ρ_w is the liquid water density. One can derive liquid water path through retrievals of optical depth and effective radius, [Petty, 2006]. A further implication of this relationship is that the precipitation (hydrological cycle) and the radiation of the Earth system is closely connected through *Re*, and that *Re* serves to be an important climate variable in the Earth's climate system.

1.1.3 Terra Satellite Platform

In an effort to provide long-term measurements of the Earth system, NASA launched its Earth Observing System (EOS) in the 1990s - a series of coordinated polar-orbiting satellites designed to monitor and understand key components of the climate system and their interactions through long-term global observations (https://eospso.nasa.gov/). Terra, as the EOS Flagship, was the first satellite to study the Earth system science, exploring the connections between Earth's atmosphere, land, snow and ice, ocean, and energy balance to understand Earth's climate and climate change and to map the impact of human activity and natural disasters on communities and ecosystems. Launched on December 18, 1999, the Terra satellite and its five onboard sensors have been continuously collecting data of the Earth's system over the past 18 years, and it is currently one of the longest single-platform satellite records for studying the Earth's system. Terra is in a sun-synchronous orbit and has an equator-cross time of 10:30 A.M. Local Standard Time. In this research work, we use two instruments both onboard Terra, namely MODIS and MISR.

The MODerate Resolution Imaging Spectroradiometer (MODIS) [Barnes et al., 1998] is a key instrument onboard the Terra satellite platform. It measures radiance in 36 discrete spectral channels from 0.4 to 14.4 μm and has a viewing swath of ~2300km in the cross-track direction. MODIS has a ground sampling resolution from 250m to 1km depending on channel. MODIS covers the entire Earth surface every 1-2 days. MODIS retrieves *Re* using bi-spectral method, with one channel from a visible or near-infrared channel that has tiny water absorption and is sensitive to optical depth, and another channel from a shortwave infrared channel (e.g., 1.6, 2.1, and 3.7 μm) that has strong water absorption, which is sensitive to *Re* [Platnick et al., 2003]. These multi-spectral retrievals of MODIS are therefore labelled as $Re_{1.6}$, $Re_{2.1}$ and $Re_{3.7}$.

The Multi-angle Imaging SpectroRadiometer (MISR) also onboard the Terra satellite is a unique instrument of its own kind: with a camera set of 9 different view angles, MISR provides 9 different views of the same scene within 7 minutes as the Terra satellite moves along track. The nadir camera (AN-camera) has a view-zenith angle of 0°, while the oblique cameras facing the along-track are designated as AF, BF, CF and DF with view zenith angles of 26.1°, 45.6°, 60° and 70.5°, respectively; and the after-track pointing cameras AA, BA, CA and DA are at view zenith angles of -26.1°, -45.6°, -60° and -70.5°, respectively. Each camera contains four spectral channels at these following wavelengths: 446nm, 558 nm, 667nm, 866nm. The MISR instrument has a swath of ~380km and it overlaps with the center of the MODIS swath. MISR projects the retrieved radiances onto the Space-Oblique Mercator (SOM) grid at resolutions from 275m to 1.1km depending on both the camera and spectral channel. The near-infrared (NIR) radiance used in this study is provided at 1.1 km with oblique cameras and 275m at AN-camera. More details of the MISR instrument design can be found in Diner et al., [1998].

1.2 Motivation

1.2.1 Current Situation for Aircraft and Satellite retrieved *Re*

Over the past 50 years, there has been various in situ measurements of *Re* from aircraft observations. It is worth noting that the focus of this research is the *Re* in marine regions, and that the continental regions are not taken into our analysis. Shown in Table 1.1 is the results from a survey conducted by Miles et al., [2000] that studied the field observations of various cloud microphysical properties of marine clouds over the past 50 years. From all the field observation results given in Table 1, a rough estimate of a typical *Re* value for marine clouds should be somewhere around 4-15 μm.

Table 1.1 Marine stratocumulus cloud observations from Miles et al., [2000].

TABLE 1. Marine clouds. Observations and results of calculations from observations of various microphysical properties and parameters of modified gamma and lognormal distributions for marine stratocumulus clouds. For data of type e, $N_{r,\mathrm{obs}}$, $\mathrm{LWC}_{\mathrm{obs}}$, and $D_{e,\mathrm{obs}}$ were reported, from which the other parameters were calculated. Similarly, for data of type m, $N_{r,\mathrm{obs}}$, $\mathrm{LWC}_{\mathrm{obs}}$, and $D_{m,\mathrm{obs}}$ were reported. Type s indicates that spectra were presented, from which the moments and parameters were calculated. Datasets indicated by * were misclassified, as judged by their total number concentration profiles.

Source	Remark	Base (m)	Top (m)	Height (m)	Type	$N_{r,\mathrm{obs}}$ (cm^{-3})	$D_{m,\mathrm{obs}}$ (μm)	$\sigma_{v,\mathrm{obs}}$ (μm)	$\mathrm{LWC}_{\mathrm{obs}}$ ($\mathrm{g\ m}^{-3}$)	$D_{e,\mathrm{obs}}$ (μm)	υ_{gam}	$D_{n,\mathrm{gam}}$ (μm)	$\sigma_{\log}$	$D_{n,\log}$ (μm)
Albrecht et al. 1995 (Fig. 8)	Marine air	630	860	650	e	50	16.8	4.3	0.15	19.0	15.6	1.1	0.24	16.4
(Azores/Madeira Islands)	Marine air	630	860	750	e	45	19.8	5.6	0.23	23.0	12.5	1.6	0.27	19.2
	Marine air	630	860	850	e	45	22.5	7.0	0.35	26.8	10.5	2.1	0.29	21.6
Duda et al. 1991 (Fig. 1)	Marine air	800	1000	800	e, m	50	15	6.5	0.04	20.0	0.8	7.0	0.74	5.0
(San Nicholas Island) flight 5	Marine air	800	1000	900	s	75	15.9	7.9	0.28	22.4	5.2	3.1	0.40	15.1
	Marine air	800	1000	1000	e, m	100	20	8.8	0.49	26.0	3.7	4.6	0.46	15.4
Duynkerke et al. 1995 (Fig. 7c)	Nocturnal stratus	240	760	240	s	23	8.0	3.4	0.01	11.5	4.2	1.8	0.43	7.2
(Azores/Madeira Islands)	Nocturnal stratus	240	760	440	s	56	15.0	4.8	0.13	17.9	10.6	1.4	0.29	14.5
	Nocturnal stratus	240	760	620	s	111	17.4	4.8	0.37	19.6	17.5	1.0	0.23	17.1
Fox and Illingworth 1997 (Fig. 1)	Typical Sc				s	91	15.2	2.3	0.18	15.9	44.6	0.3	0.15	15.0
Korolev and Mazin 1993 (Fig. 3)	Sc			1300	s	66	15.0	3.5	0.13	16.4	24.6	0.6	0.19	14.1
(St. Tallin, Russia)	Sc DDCZ			1300	s	22	13.1	4.0	0.03	15.2	13.2	1.0	0.26	12.8
Martin et al. 1994 (Fig. 1)	Sc	610	960	700	e	160	8.7	3.8	0.09	12.0	5.2	1.7	0.40	8.1
(coast of California)	Sc	610	960	800	e	182	13.7	4.0	0.31	16.0	11.9	1.1	0.28	13.2
	Sc	610	960	930	e	158	16.6	4.7	0.47	19.2	12.6	1.3	0.27	16.0
Martin et al. 1994 (Fig. 3a)	Sc	1290	1460	1310	s	107	7.1	2.3	0.03	8.6	8.8	0.8	0.32	6.7
(South Atlantic)	Sc	1290	1460	1340	s	142	8.5	2.6	0.06	10.2	10.4	0.8	0.29	8.3
	Sc	1290	1460	1390	s	143	11.4	3.3	0.14	13.3	12.4	0.9	0.27	11.1
	Sc	1290	1460	1430	s	140	13.7	3.5	0.22	15.3	17.5	0.8	0.23	13.4
Martin et al. 1994 (Fig. 12)	Scud			310	s	12	11.3	5.0	0.02	15.5	5.6	2.0	0.39	10.6
(Azores/Madeira Islands)	Scud			380	s	5	9.6	4.6	0.004	14.4	3.8	2.5	0.45	8.7
	Sc	420	730	460	s	28	15.3	6.5	0.08	19.8	7.4	2.1	0.34	14.8
	Sc	420	730	530	s	39	14.9	8.3	0.13	22.4	4.4	3.5	0.42	14.4
	Sc	420	730	610	s	59	14.3	8.6	0.20	22.6	3.8	3.9	0.45	13.6
	Sc	420	730	690	s	73	11.7	8.1	0.17	21.9	2.4	5.0	0.54	10.6
Nicholls 1984 (Fig. 6)	Sc	380	830	480	s	79	13.5	5.4	0.16	17.8	6.3	2.1	0.37	12.7
(North Sea)	Sc	380	830	730	s	94	20.8	7.0	0.59	24.9	11.0	1.9	0.29	20.2
*Noonkester 1984 (Fig. 4a)	Uniform stratus	408	684	345	m, s	194	1.7	1.7	0.003	5.3	0.9	1.8	0.72	1.4
(130 km southwest of San Diego)	Uniform stratus	408	684	426	m, s	260	4.0	3.3	0.03	9.3	1.5	2.7	0.64	3.4
	Uniform stratus	408	684	575	m, s	296	9.6	4.0	0.22	12.9	5.9	1.6	0.35	9.3
	Uniform stratus	408	684	682	m, s	228	11.5	4.8	0.29	15.5	5.8	2.0	0.39	10.7
Ryan et al. 1972 (Fig. 8)	Stratus	410	740	410	s	116	8.5	1.9	0.04	9.5	15.8	0.5	0.24	8.2
(west of Santa Cruz)	Stratus	410	740	580	s	123	15.2	4.5	0.29	18.0	10.6	1.4	0.29	14.6
	Stratus	410	740	740	s	149	16.0	5.4	0.35	19.6	8.0	1.8	0.32	15.2
Stephens and Platt 1987 (Fig. 6b)	Thin, precipitating Sc	1680	2350	1770	e	58	11.6	4.5	0.07	15.0	6.8	1.7	0.36	10.9
(off east coast of Australia)	Thin, precipitating Sc	1680	2350	1890	e	40	13.5	5.5	0.08	18.0	6.0	2.3	0.38	12.7
	Thin, precipitating Sc	1680	2350	2040	e	30	14.0	8.4	0.10	24.0	2.8	5.0	0.51	12.6
	Thin, precipitating Sc	1680	2350	2200	e	26	14.1	8.5	0.09	24.4	2.7	5.2	0.51	12.7
Stephens and Platt 1987 (Fig. 6c)	Thin Sc	1310	1980	1250	e	40	15.3	6.5	0.12	20.8	5.5	2.8	0.38	14.3
(off east coast of Australia)	Thin Sc	1310	1980	1400	e	32	15.7	7.8	0.12	23.4	4.1	3.6	0.44	14.4
	Thin Sc	1310	1980	1620	e	52	18.3	7.5	0.26	24.4	6.0	3.0	0.37	17.2
	Thin Sc	1310	1980	1830	e	35	16.6	7.9	0.15	24.2	4.4	3.8	0.43	15.3

Since the 1980s there has been efforts to study the clouds from satellite measured radiances [Schiffer and Rossow, 1983], and it has been ~30 years since satellite started taking measurements of cloud microphysical properties. Currently, all operational satellite retrievals of cloud optical properties from scattered solar radiances assume one-dimensional radiative transfer (1D-RT), where clouds and boundary conditions are treated as horizontal homogeneous (i.e., plane-parallel) planes and cloud layers vertically homogeneous. This assumption reduces radiative transfer from three dimensions (3D) to one dimension (1D, in the vertical direction), which simplifies solving the radiative transfer equation. However, this assumption can sometimes be problematic depending on the application (More discussion of 1D-RT in the next chapter). Presently there are a variety of available satellite-derived *Re* products. While some of these products are based on MODIS-like

instruments such as the Advanced Very High-Resolution Radiometer (AVHRR) [Rossow and Schiffer, 1991] that also make use of the bi-spectral method to retrieve *Re*, some are based on polarization measurements [Deschamps et al., 1994] or multi-angle measurements [Poulsen et al., 2011].

1.2.2 Intercomparison of various satellite retrieved *Re*

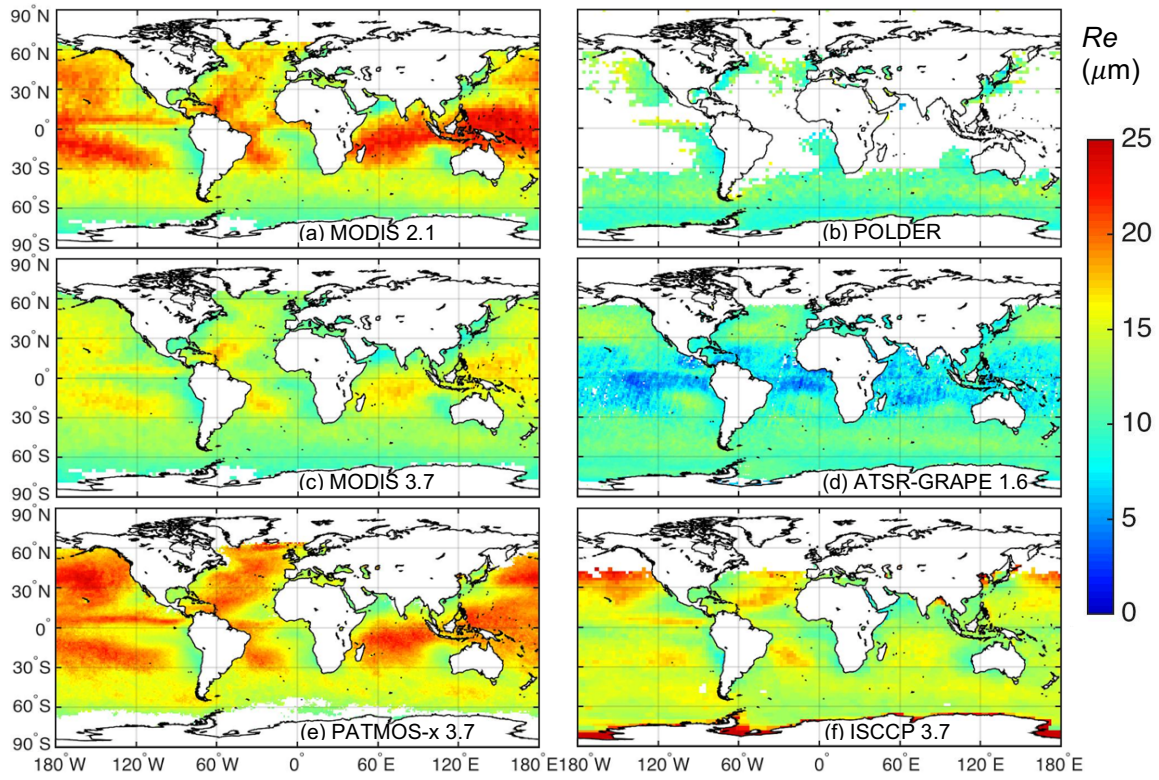

Figure 1.1 Comparison of (a) MODIS *Re* 2.1 μm, (b) POLDER *Re*, (c) MODIS *Re* 3.7 μm, (d) ATSR-GRAPE *Re* 1.6 μm, (e) PATMOS-x *Re* 3.7 μm and (f) ISCCP *Re* 3.7 μm retrieved global distribution of *Re* for multiple years mean of January.

Shown in Figure 1.1 are multiple years of January mean *Re* global distributions from MODIS 2.1 μm spectral channel, MODIS 3.7 μm spectral channel, PATMOS-x 3.7 μm spectral channel, ISCCP 3.7 μm spectral channel, ATSR-GRAPE 1.6 μm spectral channel and POLDER retrievals. Over the past there has been comparison between these available satellite-derived *Re* products [e.g., Sayer et al., 2011; Breon and Doutriaux-Boucher, 2005; Stubenrauch et al., 2012] revealed disparities that range from ~2 - 3 μm by average and up to ~8 - 9 μm between different satellite *Re* products.

On comparing the details of the various satellite-derived global distribution of *Re* given in Figure 1.1, note that these different satellite products were using different retrieval methods (e.g., while MODIS, PATMOS-x, ISCCP were using the aforementioned bi-spectral technique, POLDER take polarization measurements), come from different time periods and have different equator-crossing time. Still, they show distinct discrepancies (e.g., the difference between PATMOS-x *Re* 3.7 μm and ATSR-GRAPE *Re* 1.6 μm can be up to ~15 μm). According to a report from Ohring et al., [2005], in order for satellite instruments to detect slight changes of climate forcing signals over a long time period, the required uncertainty for passive satellite sensor retrieved *Re* is ~ 5%. A previous study from Slingo, [1990] suggests that the top-of-atmosphere radiative forcing by doubled carbon dioxide concentrations can be balanced by relative increases of ~15-20% in the amount of low clouds, and 20-35% in liquid-water path, and by decreases of 15-20 % mean drop radius), which indicates that a minimum relative accuracy of ~5% is needed to estimate climate response by monitoring *Re* over extended periods from satellite platforms.

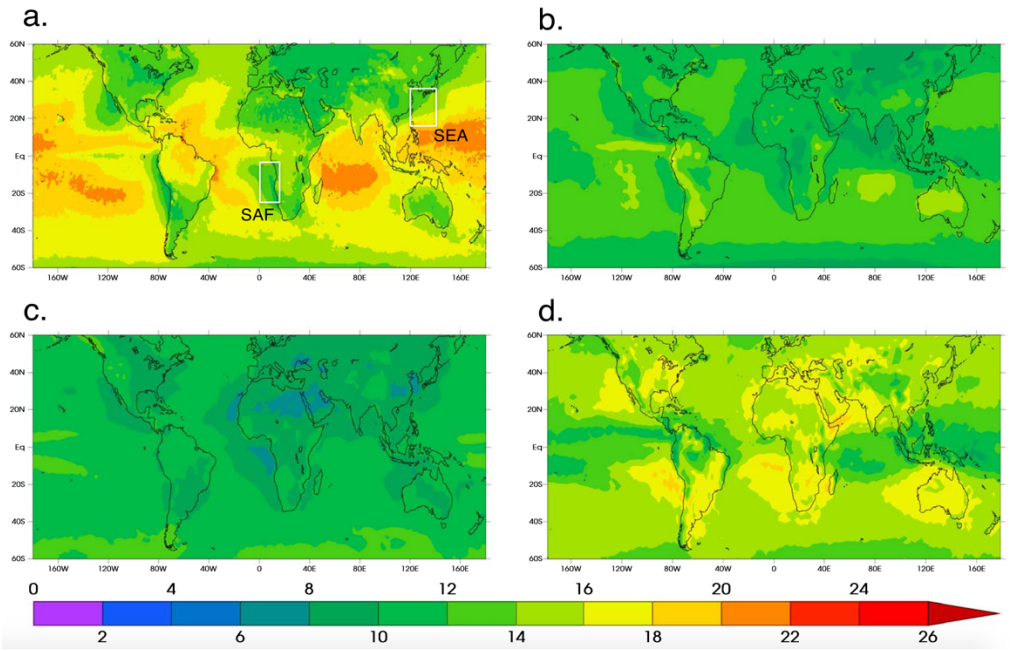

Figure 1.2 Comparison between (a) MODIS *Re* retrieval with (b) AM3, (c) CAM5 and (d) ModelE2 results from Ban Weiss et al., [2014].

At the same time, however, these satellite *Re* retrievals are often used to validate climate model performance. Like shown in Figure 1.2, Ban Weiss et al., [2014] made a comparison of the *Re* from MODIS observation against model results from the AM3, CAM5 and ModelE2. Surprisingly, not only does the model results behave quite different from the satellite retrievals, the model spread between different models is quite large. Since cloud is the largest source of uncertainty in our climate models, it is very important to understand the accuracy and error characteristics of the satellite-derived cloud products to improve the accuracy of climate model predictions. This study will be focusing on studying the regional bias of MODIS retrieved *Re* products, but will also compare the MODIS retrieved *Re* with other satellite-derived *Re* products to examine the characteristics of current MODIS-like retrievals, and to further understand the actual global distribution of *Re*.

1.2.3 Issues in MODIS *Re* retrieval approach

Given the *Re* retrieved from different satellite platforms in Figure 1.1, it is hard to find an agreement among different satellite retrieved *Re* on the global distribution of *Re*. Being one of the most popular satellite *Re* products currently available, MODIS *Re* has been used in various studies such aerosol-cloud interactions [e.g., Myhre et al., 2007; Ban-Weiss et al., 2014], cloud microphysical parameterization in climate models [e.g., Otkin and Greenwald, 2008]. On the other hand, the popularity of MODIS *Re* products have led to numerous studies that compared satellite retrieved *Re* with field observations and model simulations, and suggested hypotheses on the leading factors that may contribute to the errors and biases associated with the satellite retrieval of *Re*.

Long known is the discrepancy observed between the multi-spectral *Re* retrievals 1.6, 2.1 and 3.7 μm) from MODIS. One possible explanation suggests that the difference may be due to the vertical variation of *Re* profile and the difference in radiation penetration depth among the 3 different channels [Platnick 2000; Chang and Li, 2003]. Other studies identified cloud horizontal heterogeneity and 3-D radiative effects to be the leading sources of uncertainty in satellite retrieved *Re* [Marshak et al., 2006; Zhang et al., 2012]. It is also known that warm rain processes such as drizzle may lead to bi-modal droplet size distribution and may also lead to the discrepancies [Zhang et al., 2013; Nakajima et al., 2010].

Many studies have compared MODIS-retrieved *Re* with in-situ observations, showing that the MODIS *Re* products may carry a positive bias that vary with cloud types and sun-view geometry [e.g., Painemal and Zuidema 2011; Haney, 2013]. Yet due to the characteristics of field observations, measurements are often limited to a certain region, that these in-situ observations are

not globally representative, and it is difficult to validate satellite-retrieved *Re* in a global sense. Recently, an effort to characterize the bias in MODIS-retrieved *Re* through data fusion of the Multi-angle Imaging Spectroradiometer (MISR) and MODIS revealed biases in the zonal-mean values of MODIS-retrieved *Re* that varied from 2 to 11 μm, depending on latitude [Liang et al., 2015], and that the zonal-mean values of MODIS-retrieved *Re bias* shown dependence on cloud types: That the maximum bias appears around latitudes where cumulus clouds contribute the most to the total cloud fraction, and the minimum bias tends to be located in regions where marine-stratocumulus clouds contribute the most to the total cloud fraction. This work presented a potential of estimating the MODIS-retrieved *Re* bias in a global sense.

1.3 Objectives

The scope of this thesis is mainly focused on studying the bias of MODIS-retrieved *Re* through careful data fusion of MISR and MODIS. Here we take the findings from Liang et al., [2015], and extend the study towards a bias-correction of MODIS-retrieved *Re* at regional scales, to give us a sense of how the actual global distribution of *Re* may look like compared to the original MODIS-retrieved *Re.*

1.3.1 Study the relationship between MODIS-retrieved *Re* bias and related factors

Part of the objective of this thesis is to study the relationship between MODIS-retrieved *Re* bias and other possible related factors. Shown from Liang et al., [2015], the zonal mean MODIS *Re* bias showed possible dependence on latitude and cloud types (minima bias around latitudes where the marine-stratocumulus clouds contribute the most to the total cloud fraction, and maxima

bias around latitudes where cumulus clouds contribute the most to the total cloud fraction). Such finding encourages us to further investigate into this matter, and to determine the relationship between MODIS retrieved *Re* bias and possible related factors. Based on our current understanding of 3-D radiative transfer and previous studies on MODIS retrieved *Re* bias, this work studies the dependency of *Re* bias on cloud type and sun-view geometry, whereas the cloud type here is determined by cloud properties including cloud heterogeneity and cloud optical depth, and sun-view geometry is characterized by latitude and solar zenith angle. Through data stratification by observed cloud properties and sun-view geometry, relationship of MODIS *Re* bias and related impacting factors is further parameterized to correct the MODIS *Re*.

1.3.2 Implementation of bias-correction on MODIS *Re* at regional scales

One key merit of this thesis is to implement a bias-correction procedure for MODIS *Re* at regional scales, to provide a global perspective of how the bias associated with MODIS-retrieved *Re* may look like in terms of magnitude and distribution, and how the corrected *Re* is distributed globally. Once the parameterized relationship between MODIS-retrieved *Re* bias and the related factors is determined, we will be correcting the MODIS retrieved *Re* according to the relationship at regional scales. By using 8 years (2001-2008) of January MISR and MODIS data, the global distribution of corrected *Re* and the MODIS-retrieved *Re* bias are provided. Comparison of the corrected *Re* alongside other satellite-derived *Re* products will further expand the discussion on the validity of using Re retrievals from MODIS-like instruments.

As for the structure of this thesis, fundamental backgrounds on the data and the theoretical basis are discussed in detail in Chapter 2. Chapter 3 introduces the data stratification and further analysis of this research, Chapter 4 will revolve around the data processing aspect of this thesis.

Results of both bias-corrected *Re* and MODIS-retrieved *Re* are presented in Chapter 5, while the discussion on the comparison with other satellite-derived *Re* products is also included. Lastly, Chapter 6 gives the final conclusion and summary of this work.

CHAPTER 2: FUNDAMENTALS

2.1 Bi-spectral Retrieval of *Re*

2.1.1 Overview of Bi-Spectral Method

The main objective of this thesis is to correct the bias associated with MODIS-retrieved *Re*, so it is quite reasonable to start with the question: How does MODIS retrieve *Re*?

There are several satellite remote sensing techniques for the retrieval of *Re*. For passive multi-spectral imaging satellite sensors such as MODIS [King et al., 1992] and the Advanced Very High Resolution Radiometer (AVHRR) [Rossow and Schiffer, 1991], *Re* is retrieved simultaneously with cloud optical depth (τ) using two shortwave spectral channels [Nakajima and King, 1990] - a technique commonly known as the bi-spectral method.

Basically, two spectral channels are chosen in the bi-spectral retrieval method, with one channel from a visible or near-infrared MODIS channel at a non-absorbing wavelength of water (e.g., 0.86 μm over ocean, 0.66 μm over land), making it sensitive to the retrieval of τ, while the other channel is at a strong water absorption wavelength in the shortwave infrared spectrum range (e.g., 2.1 μm, 1.6 μm and 3.7 μm), which is sensitive to particle size.

By running simulations of different permutations of cloud optical depth and effective radius at different sun-view geometry, one can generate a look-up table of the two channels' reflectance with different cloud optical depth and cloud effective radius values. Shown in Figure 2.1 is an example of a cross-section of a look-up table for the reflectance functions at 0.86 μm and 2.1 μm at a given sun-view geometry. While the X and Y axis gives the reflectance values for the non-absorbing wavelength (0.86 μm in this case) and the strong water absorption wavelength (2.1

μm), the gridded curves in the X direction gives the values for cloud optical depth, while the Y direction gives the values for cloud effective radius. Once this LUT is generated, it can be used to determine the values of *Re* and τ from new reflectance retrievals at the two wavelengths.

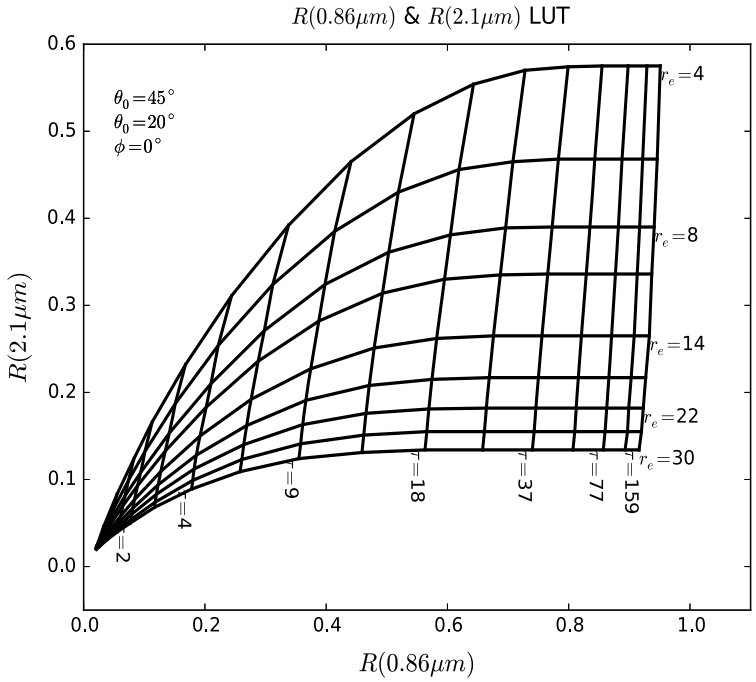

Figure 2.1 LUT for 0.86 μm and 2.1 μm Reflectance with different effective radius (*Re*) and cloud optical depth (τ) values. From Zhang et al., [2016].

2.1.2 Assumptions from Bi-Spectral Method

There are several key assumptions made in the bi-spectral method when generating the LUT. For example, the "plane-parallel" assumption assumes clouds to be horizontally homogeneous which reduces 3-D radiative transfer to 1-D radiative transfer, where the radiation field varies only in the vertical direction.

Illustrated in Figure 2.2, under the 1-D radiative transfer assumption, clouds are assumed to have the same (homogeneous) optical depth and horizontally stretch to infinity.

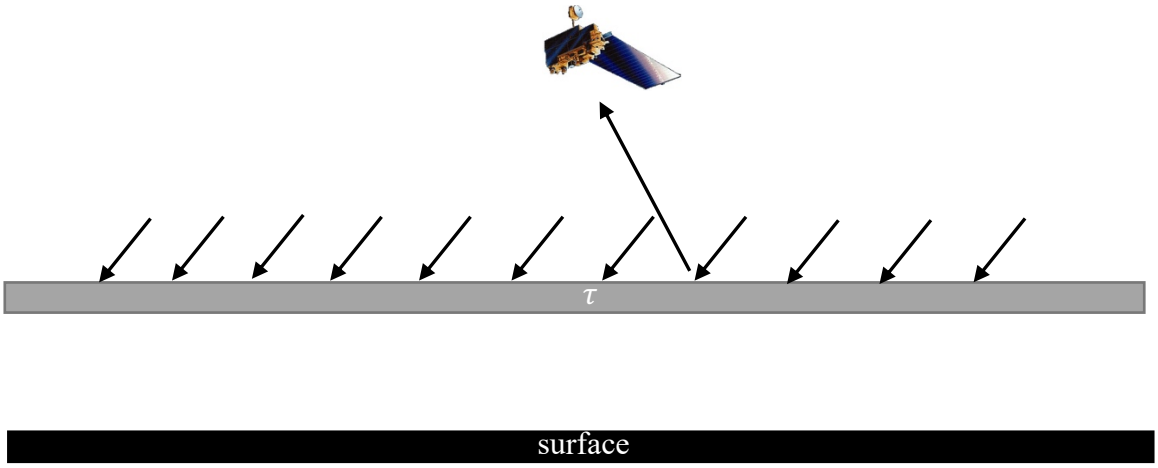

Figure 2.2 Plane parallel cloud in 1-D Radiative Transfer

Yet is this assumption good enough in approximating the clouds in nature? By looking at the clouds in nature, they are often not horizontally homogeneous over a wide range of scales, and that they could have different vertical structure as well. The radiative transfer of clouds is 3-D in reality, and this in turn would raise questions like "to what extent does the 1-D Radiative Transfer approximation produce valid accuracy for various applications?" or "when would it be most likely for the 1-D assumption to breakdown?"

While such assumption may work for homogeneous cloud fields (such as stratiform clouds under high sun conditions), for more heterogeneous and broken clouds and lower sun, however, the existence of 3-D radiative effects may lead to erroneous satellite retrievals due to the breakdown of the 1-D assumption. Studies from the past [e.g., Marshak et al., 2006; e.g., Oreopoulos and Davies, 1998] have shown the impact of 3-D effects on satellite observations, Várnai and Marshak, [2007] showed that view angle dependence of cloud optical thickness from MODIS retrievals (Figure 2.3). Given in equation 2.1 is the definition of optical depth:

$$\tau = \int \beta \, dz \qquad (2.1)$$

where β is the volume extinction coefficient and z is the path length in the vertical direction. By definition, cloud optical thickness should be independent of view angle since it is integrated in the vertical direction, yet clearly seen from Figure 2.3 is strong angular variation of cloud optical thickness from MODIS. Such finding has served as supporting evidence of 3-D radiative effects for more than two decades. In fact, the assumption that clouds are both horizontal and vertical homogeneous has been proved by several studies [e.g., Zhang et al., 2012; Dim et al., 2007; Zinner and Mayer, 2006] to lead to substantial errors in satellite retrievals of cloud properties.

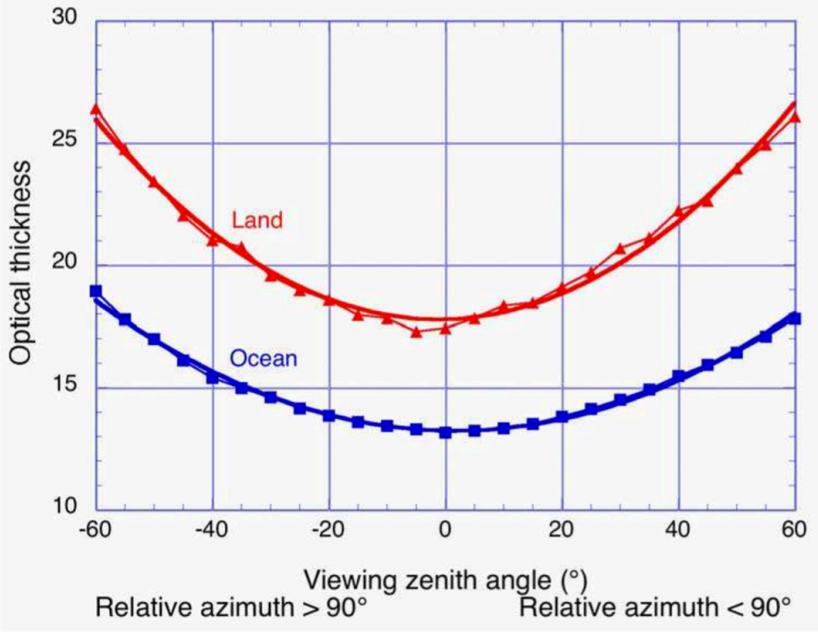

Figure 2.3 View angle dependence of mean MODIS optical thickness of inhomogeneous clouds over land and ocean. From Várnai and Marshak, [2007].

One other key assumption from the bi-spectral method is a single-mode droplet size distribution. A monomodal droplet size distribution can represent the droplet distribution for non-drizzle clouds and is mathematically convenient [Zhang et al., 2013], yet such assumption may not

fully represent the droplet size distribution of all clouds. In reality, drizzle, for example, lead to bi-modal droplet distribution, and thus can result in bias of *Re* retrievals [e.g., Minnis et al., 2004] when using the monomodal distribution assumption.

It is clear that whenever one deviates from these assumptions in our remote sensing algorithm, it leads to some form of bias in our satellite retrievals. Furthermore, it is difficult to estimate the bias associated with the breakdown of these assumptions, especially in a global perspective. For example, Di Girolamo et al. [2010] showed what the spatial patterns of 3-D radiative effects may look like, yet the impact of 3-D effects for satellite-retrieved products in a global perspective is still somewhat unknown. Therefore, it is necessary for us to study and understand the driving factors behind the satellite retrievals and try to improve the uncertainties in our satellite products.

2.2 MISR-MODIS Data Fusion

2.2.1 Data Overview

For the scope of this analysis, MISR and MODIS datasets were used and fused. Eight years of January MODIS dataset consists of the MODIS Cloud Microphysical properties (MOD06 product) and MODIS level 2 Geolocation parameters (MOD03 product). Here only liquid water clouds are considered based on the phase flag included in the Quality Assurance datafield in the MOD06 product. MODIS Cloud Effective Radius, Cloud Optical Thickness, and Horizontal Heterogeneity Index (Cloudmask_SPI) are obtained from MOD06 product. All products are given in 1km resolution. The MOD03 Geolocation parameters which include latitude and longitude coordinates of each MODIS 1km resolution pixel are used in the MODIS data re-projection aspect

of the MISR-MODIS data fusion procedure. Version 24 of MISR NIR radiance is converted to bidirectional reflectance factors (BRF) using

$$BRF = \frac{\pi L_{866}}{\cos(SZA) F_0} \quad (2.2)$$

where L_{866} is the radiance of from MISR Near-Infrared (NIR) channel retrieved at the top of the atmosphere, SZA is the solar-zenith angle and F_0 is the solar irradiance. MISR sun-view geometries at 17.6km resolution are interpolated to 1.1km resolution from Version 13 of the MISR Geometric Parameters Product (GMP). MISR Ancillary Geographic Product (AGP) is used to select clouds over ocean, it also provides the latitude and longitude coordinates for each 1.1km MISR pixel. MISR Terrestrial Atmospheric and Surface Climatology Data Version 3 are used to remove sea-ice pixels from further analysis.

2.2.2 Data Fusion Overview

Liang et al., [2009] introduced a technique of fusing MISR and MODIS data at pixel level at the cloud top, this technique serves as the basis for the data fusion approach of this thesis. This section is given to briefly summarize how this technique is implemented.

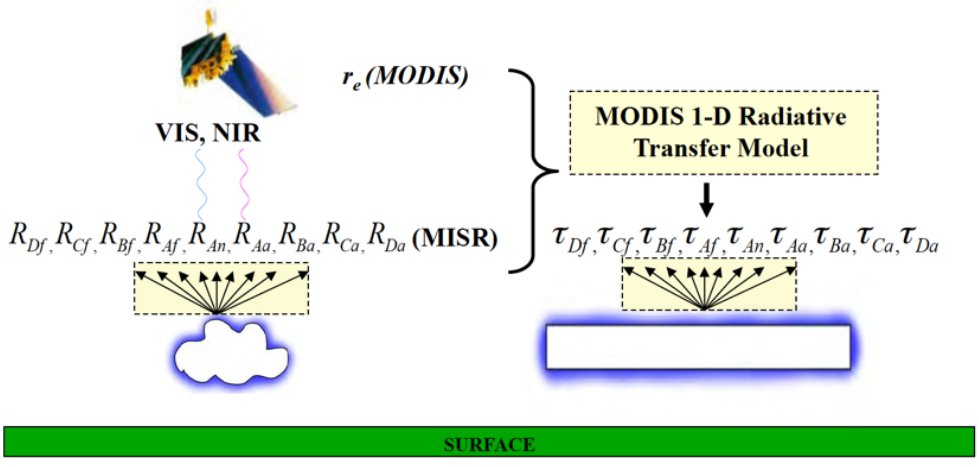

Figure 2.4 Illustration of MISR-MODIS cloud element co-registration and the retrieval of cloud optical depth at MISR 9 angle views.

For a 3 × 3 1.1km pixel domain in the MISR AN-camera image, a 3 × 3 1km MODIS retrieved cloud microphysical properties domain are projected to the MISR 1.1km SOM grid using a nearest neighbor algorithm. For the 3 × 3 1.1km domain in the MISR cameras, due to the view-angle disparity between MISR cameras, when projected onto the Earth's ellipsoid surface, the same cloud may be projected to different geolocations on the surface. To make sure that each camera has the same clouds projected to the same position, Liang et al. [2009] implemented a feature matching technique [Muller et al., 2002] that tracks the same clouds across MISR's 9 camera views at 275m resolution and register to the cloud top at the same location as the MISR AN-camera image. Following this procedure, the end result for a 3 × 3 1.1km MISR domain that is identified as fully cloudy will have cloud microphysical properties (from MODIS) registered to each pixel, as well as having 9 different view of MISR radiances (BRFs) registered to the same grid location. After this registration technique, we result in 48.2% of all fully cloudy 3×3 1.1km pixel domains that are identified as liquid water phase to be registered in all nine MISR cameras for the month of January [Liang and Di Girolamo, 2013]. The re-projected MODIS *Re* from Collection 6 Cloud Product (MOD06) [Platnick et al., 2015] are further used as inputs to DISORT [Stamnes et al., 1988] along with Version 24 of the MISR Level 1B2 near-infrared Bi-directional Reflectance Factors (BRF) to retrieve cloud optical depth at MISR 9 camera views (hereafter as MISR cloud optical depth). The details of the MISR and MODIS data fusion is explained in section 2 of Liang et al. [2009] and sections 3 and 4 of Liang and Di Girolamo [2013]. Chapter 4 in this thesis describes the MISR-MODIS co-registration procedures in detail.

2.3 Fusion Data Analysis

2.3.1 Scattering-angle dependency of Cloud Optical Depth

Liang et al., [2015] showed that when multiple-year January MODIS τ and *Re* was organized as a function of scattering angles (Θ) in terms of the deviation from the mean optical depth across 2.5° latitude bins and 1° solar zenith angle bins (Figure 2.5), they discovered an interesting dependence of both τ and *Re* - a distinct line appears in the vicinity of Θ = ~140° (the rainbow scattering direction) shows up across all latitudes as shown in Figure 2.5.

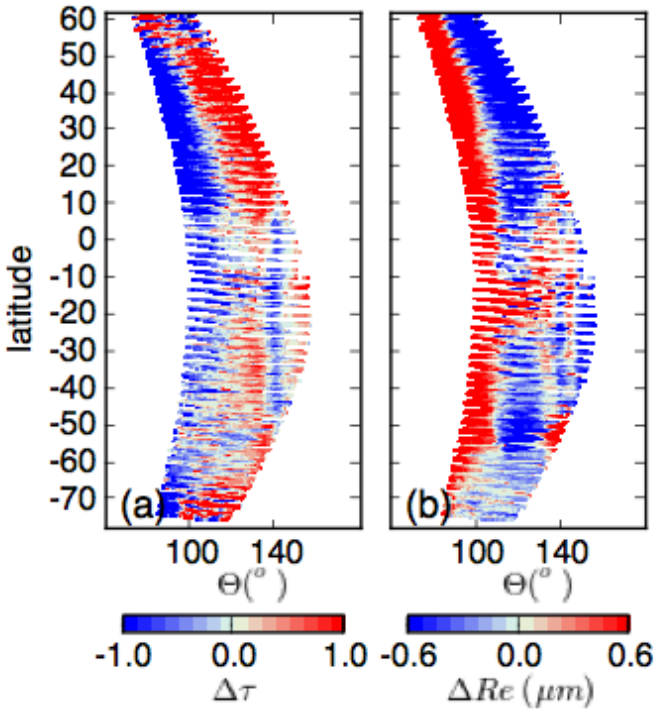

Figure 2.5 Angular Variation of MODIS τ and *Re* as a function of latitude and scattering angles (Θ), the variation is given by the deviation from the zonal mean (left: *Δτ*; right: *ΔRe*) from MODIS. From Liang et al., [2015].

When they organized the MISR 9-camera τ in the same fashion, the same distinctive line around the rainbow scattering direction also appears in the MISR τ result (Figure 2.6), which lead

to further investigation on the source of such anomaly in the optical depth retrievals. Through simulations, Liang et al., [2015] demonstrated that such angular variation of cloud optical depth observed both in MODIS and MISR can be reasonably explained by a bias in MODIS retrieved *Re*.

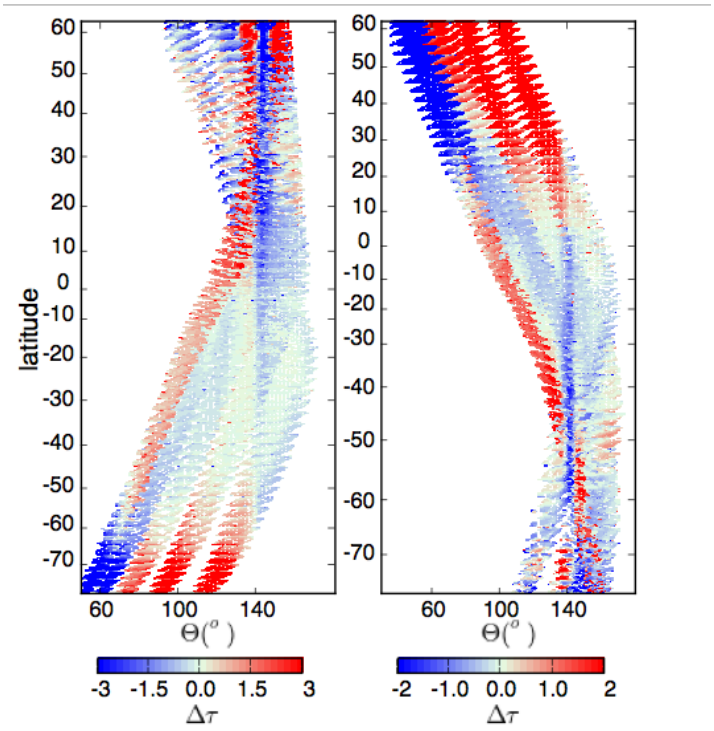

Figure 2.6 Angular Variation of MISR τ as a function of latitude and scattering angles (Θ), where the variation is given by the deviation from zonal mean cloud optical depth observations ($\Delta\tau$). from MISR Cameras (Left: Aft Cameras; Right: Forward Cameras). From Liang et al., [2015].

For example, shown in Figure 2.7 are simulations of τ as a function of scattering angles (Θ) using the Discrete Ordinates Radiative Transfer [Stamnes et al., 1988]. For a cloud with a true τ = 8 and *Re* = 10 μm, (as shown in the green curve), no angular variation of τ is observed across Θ. However, if a larger value of *Re* is used in retrieving τ, then the retrieved τ will be positively biased

relative to the truth (shown in red lines), with a local minimum in the rainbow direction, a behavior referred to as "τ-rainbow dip" in the rainbow direction (Θ=~140°). The opposite is true when a smaller *Re* is used (shown in blue lines), in other words the "*τ*-rainbow bump" at the rainbow direction. By studying the *τ* from both MISR and MODIS organized in Figure 2.5 and Figure 2.6, it is evident that the *τ* displayed a rainbow-dip behavior, which indicated the presence of a positive bias in the MODIS *Re* retrievals [Liang et al., 2015].

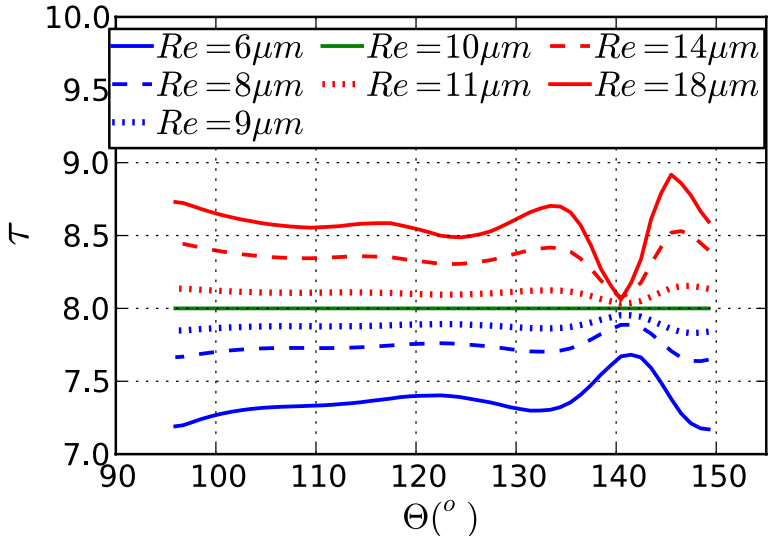

Figure 2.7 Simulations of retrieved τ across Θ as compared to the true τ = 8 and *Re* = 10 μm (green) if a smaller *Re* = 8μm and a larger *Re* = 18 μm are used instead of the true *Re* =10 μm; also plotted are the retrieved τ by using *Re* = 9 and 11 μm. From Liang et al., [2015].

2.3.2 *Fc* Analysis for *Re* Bias-Correction

To estimate the bias associated with MODIS *Re* retrievals, a correction factor, *Fc*, defined as $Re_{true} = Re_{MODIS} \times Fc$ (where Re_{true} is the corrected *Re*, and Re_{MODIS} is the MODIS-retrieved *Re*)

was introduced in Liang et al., [2015]. Shown in Figure 2.8, simulations of the deviation of optical depth ($\Delta\tau$) as a function of Θ are given for MISR aft-camera group with the input *Re* being assumed to be the Re_{true} with Fc=1.0, 0.8, 0.6, 0.4, 0.2, respectively.

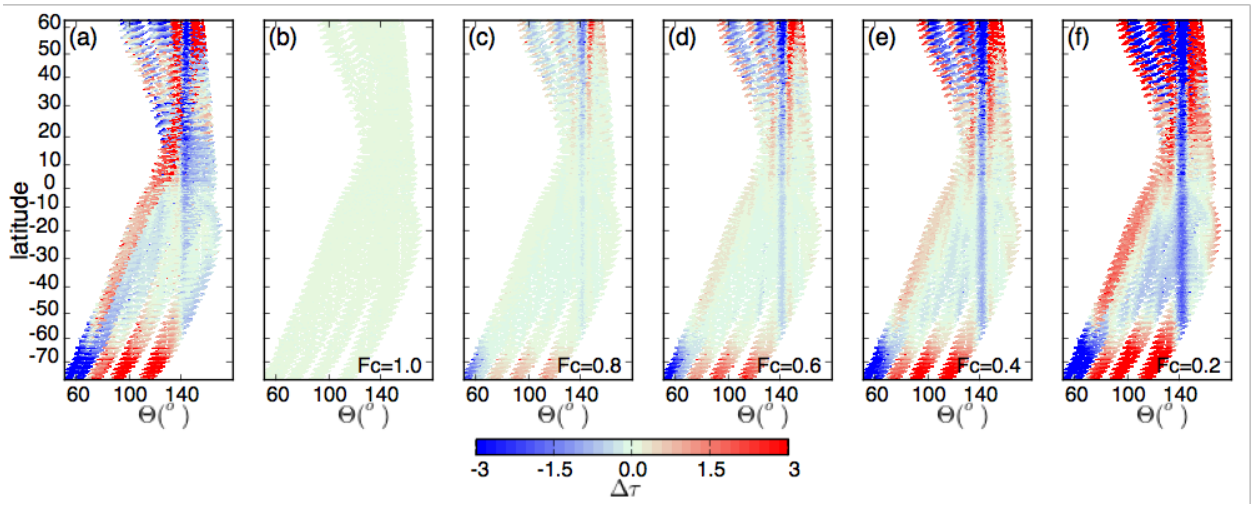

Figure 2.8 (a) Deviation of optical depth ($\Delta\tau$) as a function of scattering angles for MISR aft camera group, (b-f) $\Delta\tau$ calculated from MISR cloud optical depth with MODIS $Re_{2.1}$ (MODIS *Re* retrievals from the 2.1 μm channel) by assuming the true $Re_{true} = Re_{\mathrm{MODIS}} \times Fc$, with Fc = 1.0, 0.8, 0.6, 0.4, and 0.2, respectively. From Liang et al., [2015].

For Fc =1.0, Figure 2.8(b) shows that the τ-rainbow dip disappears as expected, since it reproduces the true τ with the same *Re* values. Yet as Fc decreases, the τ-rainbow dip becomes more and more pronounced, and a Fc range of 0.4 - 0.8 yields most similar results with the observation. Since it is discovered that the *Re* bias is related to the amplitude of the observed τ-rainbow dip, if one MISR camera observes the clouds at the rainbow direction while another MISR camera observes the cloud outside the rainbow direction, and if 1-D radiative transfer is strictly applied (optical depth is independent of sun-view geometry), the difference between the observed

optical depths of these two MISR cameras can therefore be used to determine the bias in MODIS *Re*. Yet due to the existence of 3-D radiative transfer factors (gap, concavity and bump-RAZ factors, as defined in Liang and Di Girolamo, [2013]) that are not considered in 1-D radiative transfer, such approach would lead to biased values of *Fc*, and the bias in *Fc* is dependent on different sun-view geometry, since 3-D factors can either increase or decrease optical depth with viewing obliquity, depending on the sun-view geometry [Liang and Di Girolamo, 2013]. Fortunately, MISR samples both in the rainbow scattering direction and on both sides outside the rainbow direction in many latitude bins, one can take a camera pair on one side of the rainbow dip, where *Fc* is overestimated, and another pair on the other side where *Fc* is underestimated. This allows us to bound the true value of *Fc*, but without an estimated *Fc* mean. [Liang et al., 2015]

2.3.3 Zonal mean $Re_{2.1}$ bias

Figure 2.9(a) shows the means and standard deviations of the upper and lower bound estimates of *Fc* for all eight MISR camera pairs. At each latitude bin, we can obtain both upper bound and lower bound estimates of *Fc* from camera pairs that observe within the rainbow direction and outside the rainbow direction. Note the dark shade area represent the range between the upper and lower bounds, and the lighter shade represent the range that is one standard deviation below the lower bound *Fc* mean and above the upper bound *Fc* mean. The green line links the mid-points of the upper and lower bound *Fc* mean estimates across all latitude bins (interpolated when no *Fc* retrievals are available at a latitude bin). Figure 2.9(b) shows zonal mean MODIS $Re_{2.1}$ (MODIS *Re* retrievals from the 2.1 μm channel, hereafter $Re_{2.1}$) and bias-corrected MODIS $Re_{2.1}$, and Figure 2.9(c) simply shows the zonal mean MODIS $Re_{2.1}$ bias that range from 3-11 μm. Interestingly, the distribution of the zonal mean MODIS $Re_{2.1}$ bias displayed some interesting

pattern: two local maxima of MODIS $Re_{2.1}$ bias appeared around 10°N and 35°S, cloud fractions at these latitudes are mostly contributed by marine cumulus clouds in January. At around 20°N and 25°S appears a local minima of MODIS $Re_{2.1}$ bias, and in these latitudes the marine stratocumulus clouds contributed the most to the total cloud fraction. To further study such patterns, we would need to move from zonal mean estimates towards regional estimates, and this is one of the major goals of this thesis.

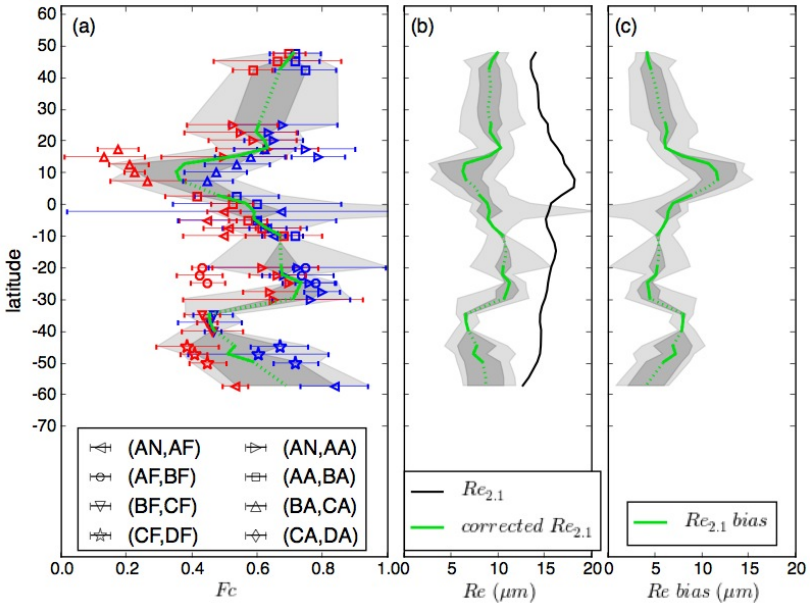

Figure 2.9 (a) *Fc* mean and standard deviation for MISR camera pairs across latitudes (b) zonal mean of MODIS $Re_{2.1}$ and bias-corrected MODIS $Re_{2.1}$ (c) zonal mean MODIS $Re_{2.1}$ bias. From Liang et al., [2015].

CHAPTER 3: METHODOLOGY

The main goal of extending the work of Liang et al., [2015] is to move from zonal mean estimates of MODIS $Re_{2.1}$ bias (Shown in Figure 2.9(c)) towards regional scale estimates which would allow us to better understand the global distribution of MODIS *Re* bias. In the process of developing a regional bias-correction estimate, we aim to further study the relationship between the MODIS *Re* bias and factors that it may depend on through data stratification.

3.1 Data Stratification

The choices of data stratification by related variables are based upon our current understanding of the possible factors that may contribute to the *Re* bias due to 3-D radiative effects: past studies have indicated that the 3-D radiative transfer effects is dependent on solar-zenith angle, cloud heterogeneity and cloud optical depth [e.g., Loeb and Davies, 1996; Zhang and Platnick, 2011; Zhang et al., 2012; Grosvenor and Wood, 2014]. Based on these findings, we choose to stratify the data by cloud types (determined by cloud heterogeneity and cloud optical depth), and the sun-view geometry (determined by latitude and solar-zenith angle).

3.1.1 Cloud Heterogeneity

The cloud horizontal heterogeneity factor (H_σ) is a metric that measures the horizontal sub-pixel heterogeneity of cloud scenes. It was introduced in Liang et al. [2009]. In this thesis it is defined as:

$$H_\sigma = \sigma / \bar{R} \quad (3.1)$$

where σ is the standard deviation and $\bar{R}$ is the mean reflectance of the 4×4 250m resolution pixels within a 1km resolution MODIS footprint. Many studies in the past have noted that MODIS retrieved $Re_{2.1}$ and $Re_{3.7}$ (MODIS *Re* retrievals from the 3.7 μm channel, hereafter $Re_{3.7}$) can have substantial differences [Zinner et al., 2010; Seethala and Horvath, 2010], and that the difference have dependence on different cloud types, $\Delta Re_{3.7\text{-}2.1}$ range from ~0 to -2 μm over coastal stratocumulus to ~-5 to -10 μm in regions of broken cumulus [Zhang and Platnick, 2011]. Similarly, Liang et al., [2015] also indicated that the MODIS-retrieved *Re* bias zonal mean distributed a comparable dependence, with smallest bias magnitude associated with latitudes where stratocumulus contributes the most to the total cloud fraction, and largest bias magnitude associated with latitudes where broken cumulus contributes the most to the total cloud fraction. All these previous results encourage us to further look into the effects of cloud heterogeneity on MODIS-retrieved *Re*, thus we are stratifying the fusion data by cloud heterogeneity.

3.1.2 Cloud Optical Depth

When it comes to classifying different cloud types, a common criterion would be the cloud optical depth (thickness) variable. For example, Rossow and Schiffer [1991] used cloud top pressure and cloud optical thickness to divide nine different cloud types from the ISCCP data. By stratifying the data further by cloud optical depth, one could simply come up with a set of different cloud types when combining the stratification by cloud horizontal heterogeneity. Furthermore, Liang et al., [2015] has discussed the mutual dependence of τ and *Re* and concluded that the observed MODIS τ rainbow-dip and MISR τ rainbow-dip (with MODIS *Re* as inputs) indicated

the overestimate of MODIS-retrieved *Re*. In a different study, Boers and Rotstayn, [2001] examined the relationship between cloud optical depth and effective radius from remote sensing observations. They concluded that depending on the relative variability of droplet concentration, cloud depth, mixing and precipitation, and the correlation between cloud depth and droplet concentration, it is possible to obtain positive, negative or zero correlation between optical depth and effective radius. Surprisingly, however, Han et al., [1998] found consistent negative correlations of optical depth with effective radius for regions of high optical depth, and positive correlations for oceanic regions of low optical depth. Here we will examine how the MODIS *Re* bias is related to the retrieved cloud optical depth, adding cloud optical depth to the stratification variables to help better characterize the different cloud types and to provide a climatology at regional scales.

3.1.3 Solar Zenith Angle

Apart from the cloud optical properties, the sun-view geometry also impacts the retrieval of cloud microphysical properties such as the *Re* and cloud optical depth [e.g., Loeb et al., 1997; Várnai and Davies, 1999]. As suggested in Grosvenor and Wood, [2014], in conditions where solar-zenith angle is larger than 65-70°, the MODIS retrievals of optical depth and *Re* becomes unreliable due to retrieval artifacts related to cloud top heterogeneity and plane-parallel bias. In particular, the mean optical depth displayed rapid increase as the solar zenith angle becomes larger than 65-70°, while the MODIS multi-spectral *Re* retrievals also distributed large spread as the solar-zenith angle became large. Other works that also looked into the impact of solar zenith angle on optical depth retrievals [Loeb et al.,1997; Loeb and Coakley, 1998; Várnai and Davies, 1999] point to the breakdown of 1-D radiative transfer assumption and the plane-parallel assumption in

the 3-D reality.

In our analysis, to determine the impact of solar zenith angle on MODIS *Re* bias, we follow the setup from Liang et al., [2015] to group the data in 2.5° latitude bins and 1° solar-zenith angle bins.

3.1.4 Stratification Procedures

MISR-MODIS Fusion Data is first stratified by 7 $H\sigma$ bins and 5 τ bins, and then further stratified into 2.5° latitude bins and 1° solar-zenith angle bins. Following the definition of *Fc* in Liang et al. [2015], *Fc* is defined as $Re_{corrected} = Fc \times Re_{MODIS,}$ the $Re_{corrected}$ is the "bias-corrected" *Re* value and Re_{MODIS} is the original MODIS retrieved *Re* value. In each 2.5° latitude bin, for each stratified data bin (stratified by H_σ bins and τ) at both the upper and lower bound, a set of *Fc* correction factors were retrieved over all possible SZA bins across all camera pairs, and a mean *Fc* is reported along with a standard deviation. In our analysis, we follow such practice to retrieve a mean *Fc* with standard deviation for each data bin (stratified by latitude, H_σ and τ). For the January data, we restricted the criteria of choosing only adjacent neighboring MISR camera pairs (e.g., AA-AN, AN-AF, BF-CF, BA-CA, …).

3.2 Trend of *Fc* as a function of H_σ and τ

Figure 3.1 shows an example of mean midpoint *Fc* (which in turn provides an estimate of the MODIS *Re* bias) as a function of τ and H_σ in 2.5° latitude bins. Larger *Fc* values (smaller correction in *Re*) are associated with smaller H_σ and τ bins (smoother and optically thinner clouds), while smaller *Fc* values (larger correction in *Re*) are associated with larger H_σ and τ. Such a

pattern with gradients shifting from large *Fc* values to smaller *Fc* values diagonally are observed for most of the latitude bins, while the magnitude of such shift varies for different latitude bins. This is consistent with our understandings of the impact of 3-D radiative effects on *Re* retrieval in the visible and IR spectrums, namely that larger *Re* bias tends to be found in more heterogeneous and optically thicker clouds due to stronger 3-D radiative effects. Such result also indicates that while *Re* bias show a dependence on cloud properties such as H_σ and τ, there is no single cloud property that dominates the behavior in MODIS-retrieved *Re* bias.

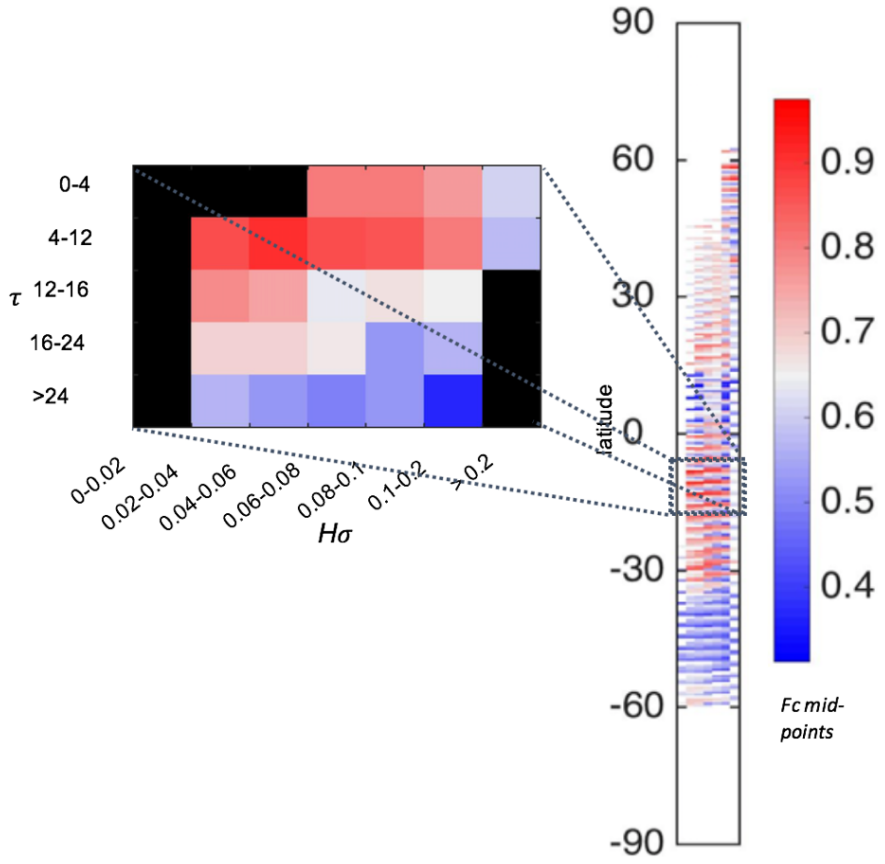

Figure 3.1 *Fc* correction factors mid-points (median values) (given as $Re_{corrected} = Fc \times Re_{MODIS}$) across all 2.5° latitude bins, each 2.5° latitude bin have *Fc* values for each H_σ and τ bins.

3.3 Parameterization of *Fc* equations

Following the data stratification discussed above, we parameterized the *Fc* equation as follows:

$$Re_{correct}(i) = Fc(i) \times Re_{MODIS}(i) \quad (3.2)$$

Where $Re_{correct}$ and Re_{MODIS} represent the bias-corrected mean *Re* value and the original mean MODIS *Re* value at 2.5° latitude and longitude resolution, *Fc* is mean of the *Fc* correction factor at the upper or lower bound at 2.5° latitude bin resolution, and *i* is the index for each stratified data bin (i = 1,2, …, 35). By keeping track of the number of samples (N) that fall into each stratified data bin, the final bias-corrected mean *Re* for each gridpoint is weighted by the number of samples:

$$Re_{w\_correct,(lat,lon)} = \sum_{i=1}^{35} \left(\frac{N_{(lat,lon)}(i)}{\sum_{i=1}^{35} N_{(lat,lon)}(i)} \cdot Re_{correct,(lat,lon)}(i) \right) \quad (3.3)$$

Where $Re_{w\_correct}$ is the weighted mean corrected *Re* at 2.5° latitude and longitude resolution, N_i is the number of sample pixels at 2.5° latitude and longitude resolution.

Following the estimates described in Liang et al., [2015], the 75% confidence level lie between the upper and lower bound estimates of *Fc*, and by assuming a Gaussian distribution, the *Fc* mid-point is equivalent to the *Fc* mean, and that the 68% confidence level within 1 standard deviation. Therefore, our standard deviation here is defined as:

$$\sigma = [(Re_{upper} - Re_{lower})/2](0.68/0.75) \quad (3.4)$$

where the Re_{upper} represent the upper bound estimate of bias-corrected *Re* and the Re_{lower} as the lower bound estimate of bias-corrected *Re*.

After such weighted mean estimate of corrected *Re*, we can provide a climatology of the mean *Re* in a global sense, that is, to provide the mean *Re* according to the contribution to the total cloud fraction of a 2.5° × 2.5° latitude-longitude bin.

CHAPTER 4: DATA PROCESSING

One of the main setbacks of this research work is the massive amount of data processing that is required. To provide a sense of how much data went into such analysis, a total of 8 years' worth of MISR-MODIS fused data for January was processed. As briefly discussed in Chapter 2, the bias-correction of MODIS *Re* is based upon the capability of MISR-MODIS Data Fusion, and the data fusion itself follows strict sequential procedures that requires co-registered pixels across both MISR camera set and MODIS to pass certain criteria. In this chapter, we will discuss the data processing procedures in detail, and also introduce the collaboration work between the University of Illinois and the Texas A&M University.

4.1 Data Processing Procedures

Following the details in the previous section, the MISR and MODIS Data Fusion features a strict serial processing procedure that is described in the following content. To implement MISR MODIS Data fusion, the following steps summarizes the working sequential steps needed for generating MISR-MODIS fusion data.

4.1.1 Data Directory Manipulation

To achieve near-automated data processing to meet up with the mass data processing demand, multiple days (at least, sometimes up to multiple years) of MISR L1B2 radiance data and MISR GMP geometric parameters along with MODIS MOD03 Geolocation dataset and MOD06 Cloud products dataset have to be organized in a common directory format so that a simple automated

search can be done by running bash scripts. To implement such data manipulation, the steps listed here are strictly followed:

1. Create a processing txt list with all valid dates of interest, path, orbit numbers, and block numbers.
2. Organize MISR L1B2 Radiance data and Geometric Parameters according to MISR path number and orbit number.
3. Organize MODIS MOD03 and MOD06 in the same fashion as the previous MISR files.

After all this is completed, a new txt list with MISR path, orbit and block information with MODIS Julian date, calendar date, MODIS 5-min block start time, start block and end block number information is generated.

Following the generation of the new txt list is the generation MODIS reprojection index. Using the geolocation information stored in MISR Ancillary Geographic Products (AGP) and MODIS MOD03 geolocation dataset, MODIS 1km pixels that overlap with MISR 1.1km pixels are re-projected to the 1.1km resolution MISR grid using nearest neighbor calculations.

4.1.2 MISR 9-camera view cloud-element co-registration

One of the key parts of the MISR-MODIS data fusion procedures is to co-locate the MISR 9 camera views to the same cloud element. By this definition, we are referring to the registration of cloud pixels across MISR's 9 camera views to the same MISR AN-camera pixel position. This process includes the identification of valid MISR AN-camera domains that pass certain criteria (will be discussed in the following sections), defining a search window to implement feature matching to track clouds across the 9 MISR camera views, and to assign the cloud pixels across MISR's 9 camera views to the MISR AN-camera pixel position.

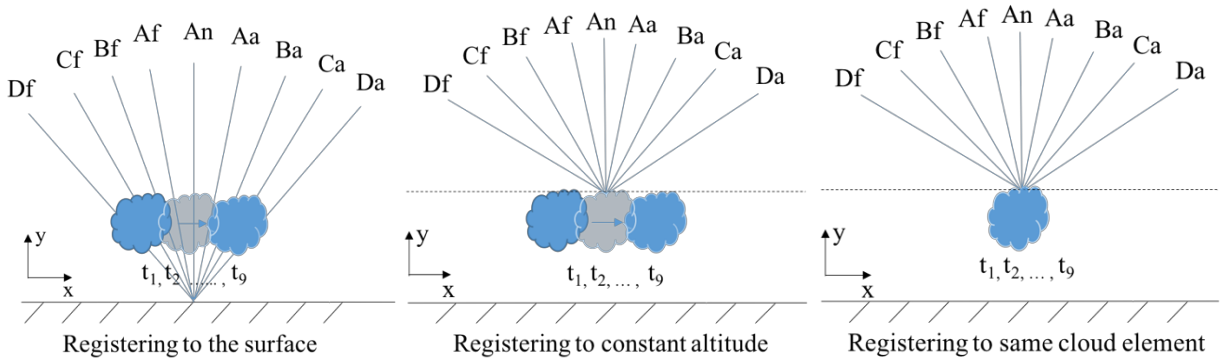

(a) (b) (c)

Figure 4.1 A schematic illustration of the co-registration of BRFs from the nine MISR cameras, each having their own time stamp (designated as t_1, t_2,… t_9) over which time the cloud can move. (a) Co-registration at the surface altitude (standard product); (b) co-registration at the cloud-top altitude; and (c) co-registration to the same cloud element.

As partially described in Chapter 1, it takes ~7 mins for all 9 MISR cameras to view the same scene, during which period due to wind effects (cloud motion, etc.) the clouds in the same scene may have moved. To avoid the cloud movement across different MISR cameras, cloud pixels are co-registered to the same geolocation as in the MISR AN camera view (Figure 4.1). More detailed information on the MISR Image Matcher techniques used in the feature matching is provided in Muller et al., [2002]. Again, the cloud-element co-registration process is divided into the following major steps:

1. Dumping MISR NIR Radiance from MISR L1B2 files into binary format in a 5-block chunk form. This 5-block defines the feature matching range that is required in the following steps.
2. Identifying valid MISR AN-camera domains that (a) has valid retrievals from all MISR 9 cameras; (b) are liquid clouds; (c) over ocean; (d) has valid MODIS reprojection index.
3. Calculate MISR cloud-element co-registration index (utilizing feature tracking technique to co-register the MISR 9 angle views to the same position as the AN-camera projection).

According to the statistics given from Liang and Di Girolamo [2013], the quality control procedures through these steps result in a total of 48.2% of fully cloudy pixels being registered for January.

4.1.3 MISR and MODIS products reprojection

After the co-registration index are generated, alongside the MODIS reprojection index, the 1km resolution MOD06 cloud products, 9-angle MISR solar-view-geometries, and MISR Near Infrared BRF can be registered to the 1.1km resolution MISR grid. For the purpose of studying the bias of MODIS-retrieved *Re*, MODIS *Re* was used as inputs to the Discrete Ordinates Radiative Transfer DISORT [Stamnes et al., 1988] model to retrieve MISR 9 angle views Cloud Optical Thickness.

4.2 Data Deliveries for Texas A&M

Through the development of this MISR-MODIS Data Fusion dataset, we combined quite a few standard data products from both MISR and MODIS, and created a fused dataset that is co-registered and overlapping. In some sense, we created a unique dataset that can be used for studies that involves utilizing the angular signatures that MISR samples and the spectral signatures that MODIS samples. One use case for such dataset is the collaboration work between Texas A&M and the University of Illinois, where they studied the ice crystal surface roughness from multi-angular sensors. The MISR-MODIS Data Fusion data is a great match for their study, since the cloud-element co-registration allows one to study the angular variation of BRF for the same cloud pixels.

For demonstration, Figure 4.2 shows the angular distribution of MISR Near InfraRed (NIR) BRFs (0.866 μm channel) averaged over a domain of 3x3 1.1 km pixels from a portion of thick cirrus using cloud element co-registration and constant altitude co-registration. It is apparent that a large discrepancy in the angular distribution of BRFs exists between the two co-registration methods. In this case, the domain was selected over the brightest portion of the thick cirrus from the nadir view. The darker pixels neighboring the bright region may be viewed from oblique angles for the constant altitude co-registration and, hence, averaged into the domain, leading to lower NIR BRFs values than those from the same cloud co-registration.

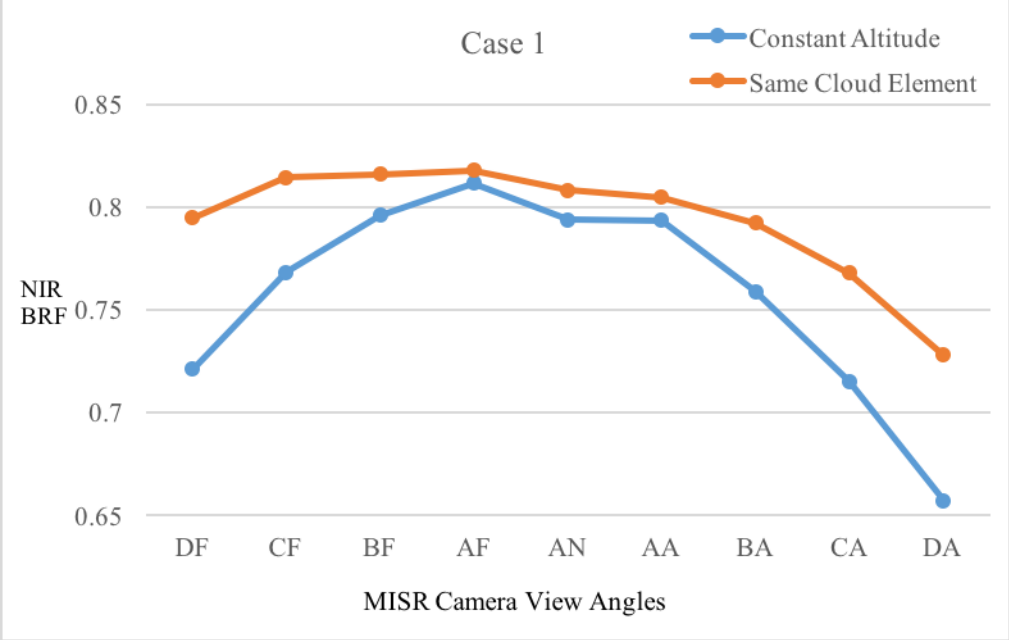

Figure 4.2 Angular distribution of BRFs averaged over a domain of 3x3 1.1km pixels from a scene (MISR Orbit 73138, Block 69) dominated by thick cirrus registered to the same cloud (orange line) and to a constant altitude (blue line). The domain is selected over the brightest portions of the cirrus.

Furthermore, this fusion dataset not only includes the MISR 9 angular Radiance retrievals, but also the MODIS cloud optical properties (such as *Re*, Cloud Top Pressure, Cloud Optical

Thickness, …) from MOD06 products, which are useful parameters for the retrieval of ice crystal roughness. Starting from March 2016, we have been providing several data deliveries for Texas A&M for their development of the ice crystal roughness retrieval algorithm. Among these data deliveries, the most notable one is the last data delivery, where the full 2013 calendar years' worth of MISR-MODIS Data Fusion was processed and delivered to Texas. Not only does this MISR-MODIS fused data covers the full year of 2013, which makes it the longest continuous timespan for MISR-MODIS fused data, it also includes the highest amount of different datafields from both MISR and MODIS products. For example, within the dataset you may find MISR L1B2 radiances for the 9 angles, MODIS L1B Band 2 and Band 7 Radiances at 1km resolution, both MISR and MODIS Cloud Top Height, MODIS Effective Radius and Cloud Optical Thickness, etc. See Appendix for a full list of the datafields stored in the 2013 dataset. In total, multiple-parallel jobs with a total of 23.4K node hours over ~1 full month time period was used to generate ~50TB of data on Blue Waters for the 2013-year dataset.

CHAPTER 5: RESULTS

5.1 MODIS original $Re_{2.1}$ and Corrected $Re_{2.1}$

Figure 5.1(a) shows the mean MODIS $Re_{2.1}$ averaged over 8 years (2001-2008) for marine liquid clouds after cloud-element registration. (Note that ~48.3% of the original MODIS cloudy pixels passed quality control procedures.) From Figure 5.1(a), the global distribution of MODIS retrieved $Re_{2.1}$ displayed a dependence on different cloud type, while the largest mean *Re* values (~22 to 25 μm) appear in the regions where the more cumuliform clouds contributes most to the total cloud fraction (e.g., around the ITCZ), the lowest mean *Re* values (~10 to 13 μm) appear in regions where the marine-stratocumulus contribute the most to the total cloud fraction (e.g., off the west coasts of continents). The global mean MODIS $Re_{2.1}$ value range from ~10 to 25 μm.

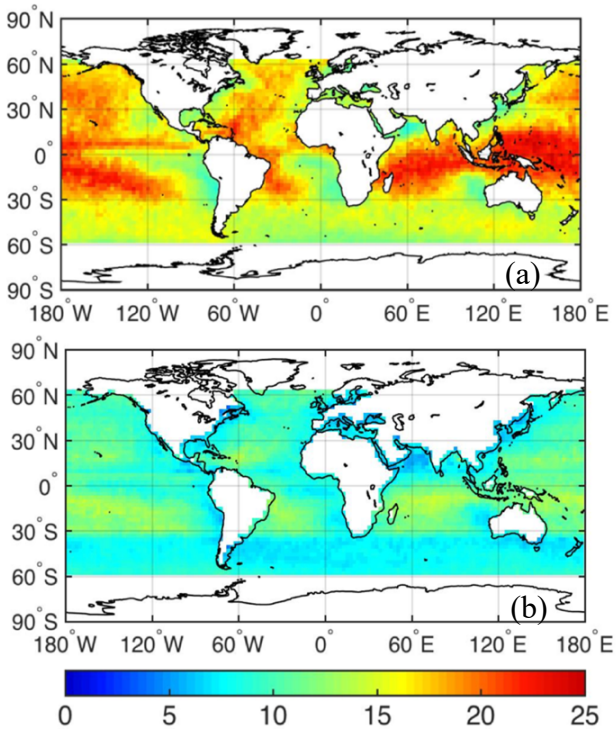

Figure 5.1 (a) mean MODIS $Re_{2.1}$ for January 2001-2008; (b) mean bias-corrected MODIS $Re_{2.1}$ using the midpoint of *Fc* upper and lower bounds for January 2001-2008.

After removing the bias according to the magnitude of the rainbow-dip, however, Figure 5.1(b) indicate a dramatic drop of mean *Re* values that is ~4 to 16 μm, while the cloud dependence feature of the original MODIS-retrieved *Re* are preserved (higher mean *Re* values in more cumuliform regions and lower mean *Re* values in more stratiform regions). Despite the substantial reduction in mean *Re* magnitude between Figure 5.1 (a) and 5.1(b), effects of increased concentration of Cloud Condensation Nuclei (CCN) over the continents [Twomey and Squires, 1959] (which can lead to smaller *Re*) [Ramanathan et al., 2001] was clearly shown in both results, with smaller mean *Re* values (~4 – 8 μm) surrounding continents.

5.2 MODIS $Re_{2.1}$ mean Bias Distribution

To have a better picture of the difference between the MODIS original *Re* and the bias-corrected MODIS *Re*, for example, shown in Figure 5.2, we subtract between the MODIS original $Re_{2.1}$ and the bias-corrected MODIS $Re_{2.1}$. In other words, shown in Figure 5.2 is the distribution of the MODIS $Re_{2.1}$ mean bias for the month of January 2001-2008 from 60°N to 60°S. Figure 5.2 reveals that according to our bias-correction procedures, MODIS $Re_{2.1}$ product carries a positive bias [Liang et al., 2015] that shows dependence on different cloud regimes, ranging from 1-3 μm in the more stratiform cloud regions (e.g., the marine-stratocumulus off the western coasts of continents) and all the way up to the 10-12 μm range in the more cumuliform regions (e.g., the strip of high bias around the ITCZ). This is consistent with our own knowledge of stratiform clouds: for the more homogeneous and smoother clouds, less impact from 3-D radiative effects result in smaller *Re* bias, while cumuliform clouds suffer stronger 3-D effects due to greater cloud heterogeneity and thus result in larger *Re* bias. Also, higher bias values generally appear in the Northern Hemisphere, which may partially be due to the lower solar-zenith angles in the higher

latitudes (even though meteorological drivers, cloud patterns may also be important influential factors for the higher bias in the Northern Hemisphere). It has been long known that the solar zenith angle has clear impact on satellite retrieved cloud microphysical properties [e.g., Loeb and Davies, 1996; Grosvenor and Wood, 2014; Kato and Marshak, 2009]. At large solar-zenith angles, even for the smoother clouds, slight change in cloud texture may lead to prominent 3-D radiative effects that lead to the observed bias in the satellite retrievals.

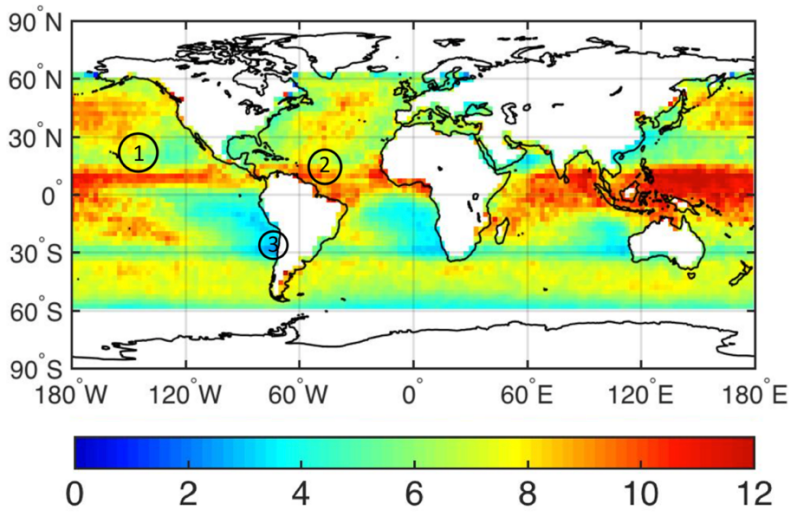

Figure 5.2 Difference between the January mean MODIS original *Re* 2.1 and the bias-corrected MODIS *Re* 2.1. The circles and descriptions indicate past field observation and model simulation results.

In search for validation of our estimates of the MODIS *Re* bias, we compare our results with some recent validations for MODIS *Re* 2.1μm. For example, in Figure 5.2, ① shows an estimate of bias ~1 to 13μm for marine boundary layer clouds under high sun condition based on MODIS-tied LES (Large Eddy Simulation) simulations [Evans, 2013]; ② indicate that according to the observations from the Rain in Cumulus over the Ocean (RICO) field campaign, bias range ~7 to 12 μm in trade cumulus regions under high sun condition [Haney, 2013]; and from the

VAMOS Ocean-Cloud-Atmosphere-Land Study Regional Experiment (VOCALS-REx) [Wood et al., 2011] ③, for stratus clouds, ~1 to 2 μm is observed under high sun condition [e.g., Painemal and Zuidema, 2011]. Figure 5.2 reveals that our estimates of the global distribution for MODIS *Re* 2.1 μm bias is in good agreement with these field validations and model simulations.

5.3 MODIS multi-spectral Original *Re* vs. Corrected *Re*

Shown in Figure 5.3 we compare the MODIS multi-spectral (2.1, 1.6, and 3.7 μm) original mean *Re* with the corrected multi-spectral mean *Re,* alongside the uncertainty associated with each multi-spectral corrected *Re*.

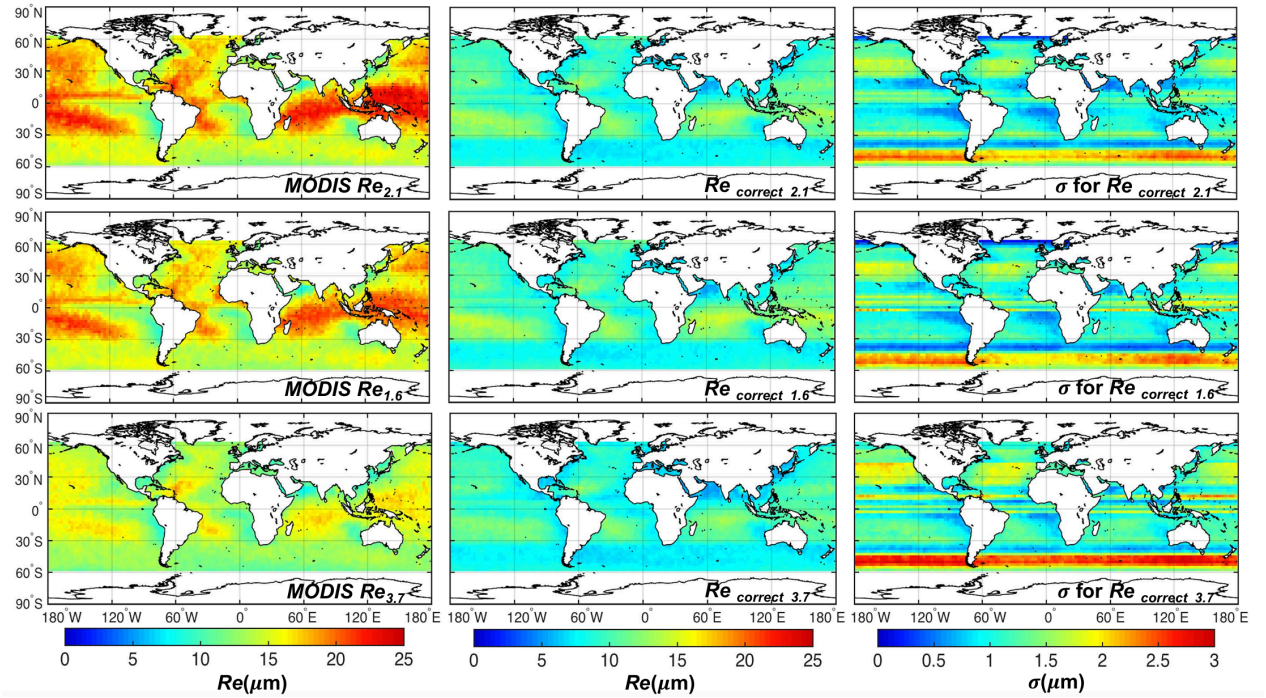

Figure 5.3 Global distribution of January mean original MODIS *Re* (Left Column), bias-corrected MODIS *Re* (Center Column), standard deviation of bias-corrected MODIS *Re* for the three MODIS spectral channels (1.6, 2.1 and 3.7 μm) (Right Column).

The first noticeable feature of Figure 5.3 is that there are substantial differences in the global distribution of mean *Re* values between the original MODIS *Re* products (e.g., MODIS retrieved *Re* from 1.6, 2.1 and 3.7 μm channel, hereafter $Re_{1.6}$, $Re_{2.1}$ and $Re_{3.7}$), especially for $Re_{3.7}$, which appears to have much smaller *Re* values across the globe than the other two *Re* products. The discrepancy between MODIS spectral retrievals of *Re* has led to studies searching for explanations. For example, Platnick [2000] showed that due to difference in the vertical distribution of weighting functions of these 3 MODIS channels ($Re_{3.7}$ peaks more to the cloud top than $Re_{1.6}$ and $Re_{2.1}$), a vertical *Re* profile that increase from cloud base to cloud top (e.g., adiabatic clouds) should have $Re_{3.7}$ greater than $Re_{2.1}$ and $Re_{1.6}$. However, Platnick also noted that the difference in weighting function of these spectral channels can only account for a difference of ~1-2 μm between the corresponding MODIS *Re* spectral retrievals, which seems insufficient to explain the discrepancy shown in Figure 5.3. Zhang et al. [2012] investigated the effects of drizzle and cloud horizontal heterogeneity on the MODIS *Re* retrievals and implied that much of the uncertainty can be attributed to 3-D radiative effects and plane-parallel *Re* bias, while drizzle does not show a significant impact on the retrieved *Re*. While our current explanation of this large discrepancy is not comprehensive, interestingly however, after we apply the bias-correction procedure to these MODIS spectral *Re* products individually, Figure 5.3 reveals that all three channels essentially showed more consensus in the mean *Re* values (they are generally within ~1-2 μm of absolute difference from channel to channel). Such difference may be more realistically the effect of the differences in the depth of radiation penetration among the spectral channels. This

tends to suggest that the corrected-*Re* might actually reflect the true *Re* value at these different wavelengths.

In estimating the bias-corrected *Re*, we also provide the uncertainty associated with the upper and lower bound estimates of the mean *Fc.* Recall that for each set of *Fc* retrieved within a 2.5° latitude bin, we separately retrieve an upper bound *Fc* mean and a lower bound *Fc* mean, the midpoint of the upper bound *Fc* mean and the lower bound *Fc* mean is used as the correction *Fc* value for correcting the MODIS *Re*. The uncertainty plot simply represents half of the distance between the upper and lower bound *Fc* retrievals (converted to μm**)**. Due to the limitation of our approach, we do see some "banding" (stratified features) artifacts. We suspect that these artifacts may be associated with sun-view geometry, since our bias-correction are based on the magnitude of the "τ-rainbow-dip", in latitudes where less MISR camera pairs can observe both sides of the "rainbow-dip", the estimate may relate to large uncertainty. Nevertheless, it is evident that all 3-channel uncertainty distribution share the dependence on different cloud regimes: it has the smallest uncertainty (~0.5 - 1 μm) around the marine-stratocumulus region where the clouds are more homogeneous, and over the rest of the world the more cumuliform cloud regimes have uncertainty ranging from ~1 - 3 μm.

5.4 Vertical Variations of *Re* from multi-spectral corrected *Re*

From Figure 5.3 we can see that after removal of the bias from the multi-spectral MODIS *Re*, we end up with similar behaviors in the mean *Re* values (that are within 1~3 μm between different channels) across all 3 MODIS spectral *Re*. Here we are interested in further quantifying the difference between the 3-channel bias-corrected MODIS *Re*. Shown in Figure 5.4, we differenced the bias-corrected global distributions of mean *Re* for the 3 channels, denoted as

$\Delta Re_{correct\_2.1\text{-}1.6}$ and $\Delta Re_{correct\_3.7\text{-}2.1}$. Upon examining the results of the difference maps (i.e. $\Delta Re_{correct\_2.1\text{-}1.6}$ and $\Delta Re_{correct\_3.7\text{-}2.1}$), several interesting features showed up: (1) $\Delta Re_{correct\ 3.7\text{-}2.1}$ shares the same general spatial pattern with $\Delta Re_{correct\_2.1\text{-}1.6}$, whereas the former appears to be greater in magnitude than the latter one in most parts of the world, while the latter one appears to be noisier; and (2) Both $\Delta Re_{correct\_2.1\text{-}1.6}$ and $\Delta Re_{correct\_3.7\text{-}2.1}$ appears to be positive over the more homogeneous cloud regions (e.g., marine-stratocumulus), while negative elsewhere across the 60°N to 60°S region we examined.

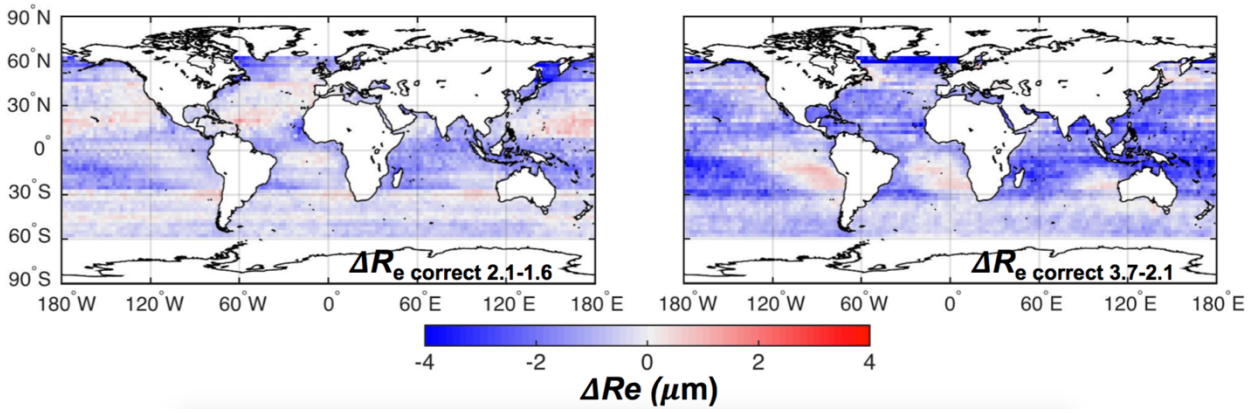

Figure 5.4 (a) Difference between the mean corrected $Re_{2.1}$ and $Re_{1.6}$ for January 2001-2008 ($\Delta Re_{correct\_2.1\text{-}1.6}$) (μm) (b) Difference between the mean corrected $Re_{3.7}$ and $Re_{2.1}$ for January 2001-2008 ($\Delta Re_{correct\_3.7\text{-}2.1}$) (μm)

If we associate these results with the aforementioned vertical distribution of weighting functions for the MODIS spectral channels, since the 3.7 μm channel weighting function peaks higher than the other two channels (2.1 μm and 1.6 μm), and that 2.1 μm peaks higher than 1.6 μm, the different signs (shown as blue and red in Figure 5.4) of $\Delta Re_{correct\_2.1\text{-}1.6}$ and $\Delta Re_{correct\_3.7\text{-}2.1}$ indicate the vertical variation of *Re* profiles near the cloud top: For instance, where $\Delta Re_{correct\_3.7\text{-}2.1}$ is positive (especially over the marine-stratocumulus regions) tends to suggest that the vertical

variation of *Re* profile may increase with altitude (e.g., adiabatic cloud profiles), and the negative holds true where $\Delta Re_{correct\ 3.7\text{-}2.1}$ is negative. We believe that this behavior indicates that the vertical variation of *Re* profiles may be related to the different types of cloud regimes, and that it may further suggest the different mechanisms of convection over the globe: For example, in some parts of the world, the dominating convection mechanism is radiative cooling from cloud top, whereas in the rest of the world, warming from below is the prominent mechanism of convection. Currently we do not have a comprehensive explanation on this matter, yet this curious finding requires further investigation.

5.5 Intercomparison of corrected *Re* with other satellite *Re* products

In Figure 5.5, we compare our global distribution of upper bound estimates of mean bias-corrected $Re_{3.7}$ for January with other satellite-retrieved *Re* datasets, namely the Pathfinder Atmospheres-Extended (PATMOS-x) [Heidinger et al., 2013] between January 2002-2008, the International Satellite Cloud Climatology Project (ISCCP) [Schiffer and Rossow, 1983] from January 1992-1999, the Along-Track Scanning Radiometers-Global Retrieval of ATSR Cloud Parameters and Evaluation (ATSR-GRAPE) [Sayer et al., 2011] from January 2003-2009, and the Polarization and Directionality of the Earth's Reflectances (POLDER) [Breon et al., 2000] from January 2006-2013. The first three dataset comes from the Global Energy and Water Cycle Experiment (GEWEX) Cloud Assessment Database [Stubenrauch et al., 2012]. POLDER Level 2 effective radius retrievals for the month of January are averaged at 2.5° resolution for direct comparison with the 2.5° resolution MODIS maps from our data analysis; for the purpose of noise filtering, for each grid point only sample numbers greater than 12 is further taken into our analysis.

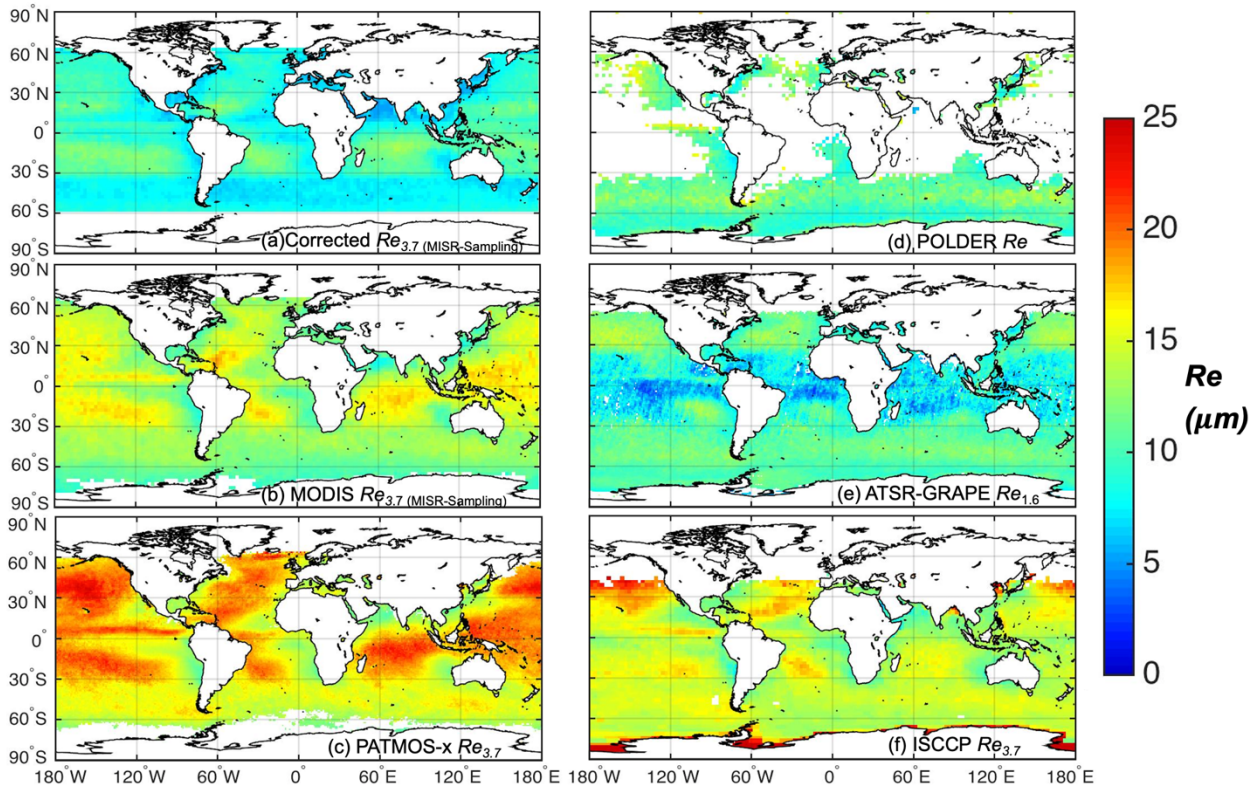

Figure 5.5 Comparison of the (a) bias-corrected MODIS $Re_{3.7}$ (with MISR sampling); (b) MODIS *Re* 3.7 μm (with MISR sampling); (c) PATMOS-x *Re* 3.7 μm; (d) POLDER *Re*; (e) ATSR-GRAPE *Re* 1.6 μm and (f) ISCCP *Re* 3.7 μm retrieved global distribution of *Re* for the multiple-years mean of January.

Before serious comparison on the details of each satellite derived *Re* product, the goal for this comparison is not to determine which product is the more accurate and reliable *Re* product, but instead, to compare these currently available satellite-derived *Re* products with the corrected *Re*, study the similarities and differences between the results while taking into account of the differences in retrieval mechanism, time of operation and other possible influential factors, to shed lights on the limitations of MODIS-like instruments (e.g., MODIS, PATMOS-x and ISCCP in Figure 5.5) using the bi-spectral retrieval technique.

From Figure 5.5, it is evident that these different satellite-retrieved *Re* products have substantial differences (e.g., the difference between PATMOS-x *Re* 3.7 μm and ATSR-GRAPE *Re* 1.6 μm can be up to ~15 μm). When compared with other satellite-retrieved *Re*, the estimated bias-corrected *Re* appears to be smaller than the other satellite retrieved monthly mean *Re* value (except for ATSR-GRAPE which gives a range of 4 – 6 μm in more cumulus cloud regions). Interestingly, the bias-corrected *Re* have magnitudes more similar to the retrievals of POLDER and ATSR-GRAPE, whereas MODIS, PATMOS-x and ISCCP result in larger *Re* retrievals than the rest. We speculate that this can be related to the fact that MODIS-like instruments using the bi-spectral technique are more susceptible to 3-D radiative effects than POLDER and ATSR-GRAPE, whereas the latter two make use of either polarization or multi-angle measurements. In terms of the implication of this comparison, it is clear that there are large discrepancies between different satellite *Re* products, while sampling differences are acknowledged, the large uncertainty associated with these satellite-retrieved *Re* products makes them questionable for conducting climate research. Furthermore, the shared features among the bias-corrected *Re*, POLDER *Re* and ATSR-GRAPE (in regions where POLDER have valid retrievals) contrast greatly to those using the bi-spectral retrieval technique (MODIS, PATMOS-x and ISCCP), and suggests that the bi-spectral technique with the 1-D radiative transfer can be problematic when retrieving *Re* in the actual 3-D world.

CHAPTER 6: DISCUSSIONS AND CONCLUSIONS

6.1 Validation

The validation of the bias-correction of MODIS-retrieved *Re* remains a significant challenge in this thesis. Primarily due to the nature of satellite retrievals, satellites have unique advantages such as high spatial coverage and wide temporal span, especially when compared to ground and field observations. In this particular case of bias-correction for MODIS-retrieved *Re*, however, the main difficulty for validation lies in the fact that the truth of MODIS-retrieved *Re*, or the true *Re* values in reality, is somewhat unknown. This may even hold true for the validation of most satellite products, since the truth of a certain satellite product is often unknown.

In the absence of the knowledge on the actual truth, field campaign measurements and ground observations serve to be one of the main sources of validation for satellite products. there are certain limitations embedded in the nature of field observations that are worth mentioning. One of such limitation is the measurement uncertainty, which simply is the same problem with satellite measurements, that the uncertainty from the in-situ measured data can lead to biased measurements, and thus undermine the validity of such observation. Another common limitation of field observation is the poor spatial and temporal coverage. Unlike satellites, field observations make use of aircrafts and in-situ sensors that can often measure at a certain location at certain periods of time, it is almost impossible to have field observations that cover the entire globe in a continuous fashion.

Despite these limitations of field observation, for the purpose of comparison and validation, this thesis compared the estimated bias associated with limited field observations that took place

in several locations across the globe during the winter seasons (to compare with the January results), as well as some model simulations. Without being impeded by the measurement uncertainties of these field observations, it is encouraging that the estimated MODIS retrieved *Re* bias were in good agreement with these field observations and model simulations (the difference are within ~1 μm). However, such validation is far from being a comprehensive validation, and that it would require more field observations and model simulation results across the different regions of the globe to increase the confidence of such validation.

6.2 Implications

Upon careful examination of the results in this thesis, several possible implications are as followed. First of all, it is evident that according to the observed "τ-rainbow dip", MODIS $Re_{2.1}$ product is associated with an overestimate that range ~ 1 to 12 μm and depend on different cloud regimes: the MODIS $Re_{2.1}$ bias range from ~1 to 3 μm over the coastal marine-stratocumulus regions, and up to ~10 to 12 μm in the broken cumulus regions. Comparison between some field observations suggest that they are in good agreement with in-situ measurements. Such estimates of the MODIS *Re* bias can help users who are currently using MODIS *Re* products to conduct research, for example, using *Re* to study aerosol-cloud interactions [e.g., Myhre et al., 2007] and cloud microphysical parameterization in climate models [e.g., Otkin and Greenwald, 2008], to acknowledge the possible existence of a systematic error within the MODIS *Re* product. Further, this could impact our current understandings of climate change, the impact of which is yet to be examined.

Finally, this result suggests that the bi-spectral retrieval method used in MODIS-like passive satellite sensors may yield to substantial errors, primarily due to breakdown of the 1-D

radiative transfer assumption and the plane-parallel assumption in the real world, whereas for satellites using other techniques, such as polarization, multi-angle measurement may not be as susceptible to 3-D effects. This would allow future satellite instrumental designs to look for alternative ways to improve the retrieval accuracy.

6.3 Limitations

A few limitations of this thesis need to be noted here. First of all, the data processing for MISR-MODIS fusion is not highly efficient, due to the code setup that requires strict sequential processing procedures, it is yet to be optimized on Blue Waters to have the capability of running in multiple-parallel jobs for each step. Such inefficient processing procedure makes it nearly impossible to implement full-mission-year data processing (consider the fact that processing 12 months' worth of data takes about 1 full months' time). One side effect of such computational speed is the amount of data processed that can be used for bias-correction estimates. Due to the limited amount of available data for the analysis, larger uncertainty and more artifacts tend to be associated with the results, and that it also limits the possibility of looking into other related topics, such as *"the seasonal variation of MODIS retrieved Re bias"*.

Another limitation lies with the methodology of the approach. This method of bias-correction can only account for the bias associated with the observed "τ-rainbow dip" near the rainbow scattering direction, but there may be other factors (such as the effect of View-Zenith Angle differences [e.g., Liang and Di Girolamo, 2013], effects of drizzle [e.g., Zhang et al. 2013] that may contribute to the bias, and the impact of which is still somewhat unknown. Furthermore, when parameterizing the bias-correction equations, the retrieval of *Fc* is set to be at every 2.5° latitude bin rather than the more logical 2.5° latitude by 2.5° longitude bin, primarily due to the

amount of computational work that is required. This stratification limitation resulted in artifacts that appeared in a few latitude bins in the results.

Finally, when considering for the uncertainty associated with the *Fc* retrievals at each 2.5° latitude bin, the practice of using the midpoints as the median of *Fc* upper bound and *Fc* lower bound seemed questionable. Since the *Fc* upper bound and lower bound estimates are both independent sets of *Fc* samples retrieved at different solar-zenith angles, the sample distribution of *Fc* from the lower to the upper bound may not strictly follow a normal distribution, so it would be questionable to approximate the midpoints as the mean of the *Fc* upper and lower bounds. More investigation into efficient representation of the uncertainties should be done.

6.4 Summary

This thesis presented a new way of quantifying the MODIS *Re* bias at regional scales. In particular, using 8 years of January MISR and MODIS fusion data, we reported estimates of bias-corrected mean MODIS $Re_{2.1}$ that range from ~4 - 16 μm depending on different cloud regimes. By comparing the upper bound estimates of the bias-corrected mean MODIS $Re_{2.1}$ and the original mean MODIS $Re_{2.1}$, we revealed that the original MODIS $Re_{2.1}$ may be overestimate by ~1 to 12 μm depending on latitude and cloud types. Through further comparison with past studies, our estimates are consistent with past in-situ field observations. Removing the bias for the MODIS multi-spectral *Re* retrievals reveal similar results (the difference between channels are generally within ~1 to 2 μm). Difference between the bias-corrected MODIS $Re_{3.7}$ and $Re_{2.1}$ showed clear dependence on cloud regimes (negative over more cumulus regions, and positive over marine-stratocumulus regions), which suggest differences in the vertical variations of *Re* profiles between the different channels. We suspect that this may be due to the different mechanisms of convection

over the globe, and this may also impact our current interpretation of the vertical profile of *Re* from MODIS [e.g., Chang and Li, 2003]. The bias-correction procedures in this work demonstrated a potential of quantifying the regional bias in MODIS *Re* associated with the plane-parallel approximation and may further be applied to other MODIS-like instruments to improve the accuracy of these satellite-derived cloud microphysical properties. In terms of final conclusions, the large uncertainties of MODIS-retrieved *Re* is far from the required 5% accuracy for climate studies [Ohring et al., 2005]. The impact of the large uncertainties to studies that use the original MODIS *Re* products to examine, for example, cloud microphysical parameterization in climate models [e.g., Otkin and Greenwald, 2008] and cloud-aerosol interactions [e.g., Ban-Weiss et al., 2014] should be examined in depth.

6.5 Future work

In terms of future work, before looking into other topics, it is necessary to start with the investigation on a good statistical representation of the uncertainty (or confidence intervals) associated with the bias-correction of MODIS retrieved *Re*. (As discussed in Section 6.3), it will be very useful if we can associate the bias-corrected *Re* estimates with a confidence interval (e.g., a 95% confidence level) to give us some idea on the range of uncertainties.

Another potential research topic is to further study the seasonal variations of MODIS retrieved *Re* bias with the additional availability of MISR-MODIS fused data for the summer months' (July or August). It would be interesting to examine the changes between the global distribution of MODIS retrieved *Re* (and bias) and investigate the possible factors that lead to such

differences. One known impacting factor is the solar zenith angle effect, since the solar zenith angle between Northern Hemisphere winter and summer are different.

One of the remaining questions of this thesis is to further investigate into the cause of the observed vertical variation of *Re* among different MODIS spectral channels. An examination into dynamics of atmospheric convection is required to determine what are the leading mechanisms of convection in different cloud regimes, and by taking in re-analysis data one could also look into the meteorological drivers that may contribute to the bias in the MODIS *Re* retrievals.

As for validation, there are currently quite a few new field campaigns on cloud microphysical and macrophysical properties such as the ObserRvations of Aerosols above Clouds and their intEractionS (ORACLES) off the west coast of Africa, and the Cloud, Aerosol and Monsoon Processes Philippines Experiment ($CAMP^2EX$) taking place in the Philippines in 2019. It would be interesting to compare and validate the estimated MODIS *Re* bias with measurements from these new field campaigns.

Lastly, the necessity of speeding up the current MISR-MODIS data processing on Blue-Waters is self-evident. Eventually the bias-correction procedures should be improved to a stage that it can be applied to a full-mission-length processing, and this would require making the maximum possible use of the parallel supercomputing power of Blue Waters.

References

Ban-Weiss, G.A., L. Jin, S.E. Bauer, R. Bennartz, X. Liu, K. Zhang, Y. Ming, H. Guo, and J.H. Jiang (2014), Evaluating clouds, aerosols, and their interactions in three global climate models using satellite simulators and observations. J. Geophys. Res. Atmos., 119, no. 18, 10876-10901, doi:10.1002/2014JD021722.

Barnes, W., T. Pagano, and V. Salomonson (1998), Prelaunch characteristics of the Moderate Resolution Imaging Spectroradiometer (MODIS) on EOS-AM1, IEEE Transactions on Geoscience and Remote Sensing, 36(4), 1088–1100, doi:10.1109/36.700993.

Boers, R. and Rotstayn, L. D. (2001), Possible links between cloud optical depth and effective radius in remote sensing observations. Q.J.R. Meteorol. Soc., 127: 2367-2383. doi:10.1002/qj.49712757709

Breon, F. M. and Colzy, S., (2000): Global distribution of cloud droplet effective radius from POLDER polarization measurements, Geo phys. Res. Lett., 27, 4065–4068.

Breon, F.M., and M. Doutriaux-Boucher (2005), A comparison of cloud droplet radii measured from space, IEEE Transactions on Geoscience and Remote Sensing, 43(8), 1796–1805, doi:10.1109/tgrs.2005.852838.

Chang, F.-L., and Z. Li (2003), Retrieving vertical profiles of water-cloud droplet effective radius: Algorithm modification and preliminary application, Journal of Geophysical Research: Atmospheres, 108(D24), doi:10.1029/2003jd003906.

Chylek, P., M. K. Dubey, U. Lohmann, V. Ramanathan, Y. J. Kaufman, G. Lesins, J. Hudson, G. Altmann, and S. Olsen (2006), Aerosol indirect effect over the Indian Ocean, Geophysical

Research Letters, 33(6), doi:10.1029/2005gl025397.

Deschamps, P.-Y., M. Herman, A. Podaire, and A. Ratier (1994), The POLDER Mission: Instrument Characteristics and Scientific Objectives, IEEE Trans. Geosc. Rem. Sens. 32, 598-615. DOI: 10.1109/36.297978

Di Girolamo, L., L. Liang, and S. Platnick (2010), A global view of one-dimensional solar radiative transfer through oceanic water clouds, Geo phys. Res. Lett., 37, L18809, doi:10.1029/2010GL044094.

Diner, D. et al. (1998), Multi-angle Imaging SpectroRadiometer (MISR) instrument description and experiment overview, IEEE Transactions on Geoscience and Remote Sensing, 36(4), 1072–1087, doi:10.1109/36.700992.

Evans, K. F. (2013). Final Report for "Estimating and Correcting MODIS 1D Retrieval Errors in Boundary Layer Clouds" (Award NNX08BA04G), Univ. of Colorado, Boulder.

Grosvenor, D. P., and R. Wood (2014), The effect of solar zenith angle on MODIS cloud optical and microphysical retrievals within marine liquid water clouds, Atmospheric Chemistry and Physics, 14(14), 7291–7321, doi:10.5194/acp-14-7291-2014.

Han, Q., W. B. Rossow, J. Chou, and R. M. Welch (1998), Global Survey of the Relationships of Cloud Albedo and Liquid Water Path with Droplet Size Using ISCCP, Journal of Climate, 11(7), 1516–1528, doi:10.1175/1520-0442(1998)011<1516:gsotro>2.0.co;2.

Hansen, J. E. (1971), Multiple Scattering of Polarized Light in Planetary Atmospheres Part II. Sunlight Reflected by Terrestrial Water Clouds, Journal of the Atmospheric Sciences, 28(8), 1400–1426, doi:10.1175/1520-0469(1971)028<1400:msopli>2.0.co;2.

Haney, C. O. (2013), Cloud drop effective radius for trade wind cumuli observed during RICO by

aircraft and MODIS MS thesis, Univ. of Illinois at Urbana-Champaign, 89 pp.

Heidinger, A.K., M.J. Foster, A. Walther, and X. Zhao, (2014). The Pathfinder Atmospheres–Extended AVHRR Climate Dataset. Bull. Amer. Meteor. Soc., 95, 909–922,https://doi.org/10.1175/BAMS-D-12-00246.1

Hong, G., P. Yang, B. A. Baum, A. J. Heymsfield, and K.-M. Xu (2009), Parameterization of Shortwave and Longwave Radiative Properties of Ice Clouds for Use in Climate Models, Journal of Climate, 22(23), 6287–6312, doi:10.1175/2009jcli2844.1.

Hubanks, P. A. (2014), MODIS Atmosphere QA Plan for Collection 006, Version 6, NASA Goddard Space Flight Center, Greenbelt, MD 20071

Kato, S., and A. Marshak (2009), Solar zenith and viewing geometry-dependent errors in satellite retrieved cloud optical thickness: Marine stratocumulus case, J. Geophys. Res., 114, D01202, doi:10.1029/2008JD010579.

King, M., Y. Kaufman, W. Menzel, and D. Tanre (1992), Remote sensing of cloud, aerosol, and water vapor properties from the moderate resolution imaging spectrometer (MODIS), IEEE Transactions on Geoscience and Remote Sensing, 30(1), 2–27, doi:10.1109/36.124212.

Liang, L., Di Girolamo, and Platnick, S. (2009): View-angle consistency in reflectance, optical thickness and spherical albedo of marine water-clouds over the northeastern Pacific through MISR-MODIS fusion. Geophys. Res. Lett., 36(9), doi:10.1029/2008GL037124

Liang, L., and L. D. Girolamo (2013), A global analysis on the view-angle dependence of plane-parallel oceanic liquid water cloud optical thickness using data synergy from MISR and MODIS, Journal of Geophysical Research: Atmospheres, 118(5), 2389–2403, doi:10.1029/2012jd018201.

Liang, L., L. Di Girolamo, and W. Sun (2015). Bias in MODIS cloud drop effective radius for oceanic water clouds as deduced from optical thickness variability across scattering angles. J. Geophys. Res., 120, doi: 10.1002/2015JD023256

Loeb, N. G., and R. Davies (1996), Observational evidence of plane parallel model biases: Apparent dependence of cloud optical depth on solar zenith angle, J. Geophys. Res., 101(D1), 1621–1634, doi:10.1029/95JD03298.

Loeb, N. G., T. Várnai, and R. Davies (1997), Effect of cloud inhomogeneities on the solar zenith angle dependence of nadir reflectance, Journal of Geophysical Research: Atmospheres, 102(D8), 9387–9395, doi:10.1029/96jd03719.

Loeb, N. G., and J. A. Coakley (1998), Inference of Marine Stratus Cloud Optical Depths from Satellite Measurements: Does 1D Theory Apply?, Journal of Climate, 11(2), 215–233, doi:10.1175/1520-0442(1998)011<0215:iomsco>2.0.co;2.

Marshak, A., S. Platnick, T. Várnai, G. Wen, and R. F. Cahalan (2006), Impact of three-dimensional radiative effects on satellite retrievals of cloud droplet sizes, J. Geophys. Res., 111, D09207, doi:10.1029/2005JD006686.

Menon, S., A. D. Del Genio, Y. Kaufman, R. Bennartz, D. Koch, N. Loeb, and D. Orilkowski (2008), Analyzing signatures of aerosol-cloud interactions from satellite retrievals and the GISS GCM to constrain the aerosol indirect effect, J. Geophys. Res., 113, D14S22, doi:10.1029/2007JD009442.

Miles, N. L., J. Verlinde, and E. Clothiaux (2000), Cloud droplet size distributions in low-level stratiform clouds, J. Atmos. Sci., 57(2), 295–311. Nakajima, T., and M. D. King (1990), Determinations of the optical thickness and effective particle radius of clouds from reflected

solar radiation measurements. Part I: Theory, J. Atmos. Sci., 47, 1878–1893.

Minnis P., Arduini, R.F., Young, D.F., Ayers, J.K., Albracht, B. and co-authors (2004). An Examination of the Impact of Drizzle Drops on Satellite-Retrieved Effective Particle Sizes, Proceedings of the 14th International Conference on Clouds and Precipitation, Bologna, Italy.

Muller, J.-P., A. Mandanayake, C. Moroney, R. Davies, D. Diner, and S. Paradise (2002), MISR stereoscopic image matchers: techniques and results, IEEE Transactions on Geoscience and Remote Sensing, 40(7), 1547–1559, doi:10.1109/tgrs.2002.801160.

Myhre, G., N. Bellouin, T.F. Berglen, T.K. Berntsen, O. Boucher, A. Grini, I.S.A. Isaksen, M. Johnsrud, M.I. Mishchenko, F. Stordal, and D. Tanre, (2007), Comparison of the radiative properties and direct radiative effect of aerosols from a global aerosol model and remote sensing data over ocean. *Tellus*, 59B, 115-129, doi:10.1111/j.1600-0889.2006.00226.x.

Nakajima, T., and M. D. King (1990): Determination of the optical thickness and effective particle radius of clouds from reflected solar radiation measurements. Part I: Theory. J. Atmos. Sci., 47, 1878–1893, doi:10.1175/1520-0469(1990)047,1878: DOTOTA.2.0.CO;2.

Nakajima, T., and M. Tanaka (1986), Matrix formulations for the transfer of solar radiation in a plane-parallel scattering atmosphere, Journal of Quantitative Spectroscopy and Radiative Transfer, 35(1), 13–21, doi:10.1016/0022-4073(86)90088-9.

Nakajima, T. Y., K. Suzuki, and G. L. Stephens (2010), Droplet growth in warm water clouds observed by the A-Train. Part I: Sensitivity analysis of the MODIS-derived cloud droplet sizes, J. Atmos. Sci.,67, 1884–1894, doi:10.1175/2009JAS3280.1

Ohring, G., et al. (2005), Satellite instrument calibration for measuring global climate change: Report of a workshop, Bull. Am. Meteorol. Soc., 86, 1303–1313, doi:10.1175/BAMS-86-9-

1303.

Oreopoulos, L., and R. Davies (1998), Plane Parallel Albedo Biases from Satellite Observations. Part II: Parameterizations for Bias Removal, Journal of Climate, 11(5), 933–944, doi:10.1175/1520-0442(1998)011<0933:ppabfs>2.0.co;2.

Otkin, J. A., and T. J. Greenwald (2008), Comparison of WRF Model-Simulated and MODIS-Derived Cloud Data, Monthly Weather Review, 136(6), 1957–1970, doi:10.1175/2007mwr2293.1.

Painemal, D., and P. Zuidema (2011), Assessment of MODIS cloud effective radius and optical thickness retrievals over the Southeast Pacific with VOCALS-REx in situ measurements, J. Geophys. Res., 116, D24206, doi:10.1029/2011JD016155.

Petty, G. W. (2006), A first course in atmospheric radiation, Sundog Pub., Madison.

Platnick, S. (2000), Vertical photon transport in cloud remote sensing problems, J. Geophys. Res., 105, 22,919–22,935, doi:10.1029/2000JD900333.

Platnick, S., M. King, S. Ackerman, W. Menzel, B. Baum, J. Riédi, and R. Frey (2003), The MODIS cloud products: Algorithms and examples from Terra, IEEE Trans. Geosci. Remote Sens., 41(2), 459–473.

Platnick, S., M. King, K. Meyer, G. Wind, N. Amarasinghe, B. Marchant, G. Arnold, Z. Zhang, P. Hubanks, B. Ridgway, J. Riedi (2015), MODIS Cloud Optical Properties: User Guide for the Collection 6 Level-2 MOD06/MYD06 Product and Associated Level-3 Datasets, 141 pp., NASA Goddard, Greenbelt, MD, USA, 2015.

Platnick, S., and S. Twomey (1994), Determining the susceptibility of cloud albedo to changes in

droplet concentration with the Advanced Very High Resolution Radiometer, J. Appl. Meteorol., 33, 334–347, doi:10.1175/1520-0450(1994)033<0334:DTSOCA>2.0.CO;2.

Poulsen, C. A., Watts, P. D., Thomas, G. E., Sayer, A. M., Siddans, R., Grainger, R. G., Lawrence, B. N., Campmany, E., Dean, S. M., and Arnold, C (2011), Cloud retrievals from satellite data using optimal estimation: evaluation and application to ATSR, Atmos. Meas. Tech. Discuss., 4, 2389–2431, doi:10.5194/amtd-4-2389- 2011.

Ramanathan, V., Crutzen, P. J., Kiehl, J. T., and Rosenfeld, D. (2001), Aerosols, climate and the hydrological cycle, Science, 294, 2119–2124.

Rossow, W.B., and R.A. Schiffer (1991): ISCCP cloud data products. Bull. Amer. Meteorol. Soc., 71, 2-20.

Sayer, A. M. et al. (2010), Global retrieval of ATSR cloud parameters and evaluation (GRAPE): dataset assessment, Atmospheric Chemistry and Physics Discussions, 10(11), 25619–25686, doi:10.5194/acpd-10-25619-2010.

Seethala, C., and Á. Horváth (2010), Global assessment of AMSR-E and MODIS cloud liquid water path retrievals in warm oceanic clouds, J. Geophys. Res., 115, D13202, doi: 10.1029/2009JD012662.

Schiffer, R.A., and W.B. Rossow (1983): The International Satellite Cloud Climatology Project (ISCCP): The first project of the World Climate Research Programme. *Bull. Amer. Meteorol. Soc.*, 64, 779-784.

Slingo, A. (1989) A GCM parameteriztion for the shortwave radiative Properties of Water Clouds, J. Atmos. Sci., 46, 1419–1427, doi:10.1175/1520-0469(1989)046<1419:Agpfts>2.0.Co;2.

Solomon, S., D. Qin, M. Manning, Z. Chen, M. Marquis, K.B. Averyt, M. Tignor and

H.L. Miller (eds.) (2007). Climate Change 2017: The Physical Science Basis. Cambridge University Press, Cambridge, United Kingdom and New York, NY, USA, 996 pp.

Song, X., G.J. Zhang, and J.F. Li (2012). Evaluation of Microphysics Parameterization for Convective Clouds in the NCAR Community Atmosphere Model CAM5. J. Climate,25, 8568–8590, https://doi.org/10.1175/JCLI-D-11-00563.1

Stamnes, K., S.-C. Tsay, W. Wiscombe, and K. Jayaweera (1988), Numerically stable algorithm for discrete-ordinate-method radiative transfer in multiple scattering and emitting layered media, Applied Optics, 27(12), 2502, doi:10.1364/ao.27.002502.

Stubenrauch, C.J., W. B. Rossow, and S. Kinne (2012), Assessment of global cloud datasets from satellites: A project of the World Climate Research Programme Global Energy and Water Cycle Experiment (GEWEX) Radiation Panel. WCRP Rep. 23/2012, 176 pp.

Stubenrauch, C.J., W.B. Rossow, S. Kinne, S. Ackerman, G. Cesana, et al. (2013), Assessment of global cloud datasets from satellites: Project and database initiated by the GEWEX radiation panel. Bulletin of the American Meteorological Society, American Meteorological Society, 2013, 94 (7), pp.1031-1049. <10.1175/BAMS-D-12-00117.1>.

Twomey, S. and Squires, P. (1959), The Influence of Cloud Nucleus Population on the Microstructure and Stability of Convective Clouds. Tellus, 11: 408-411. doi:10.1111/j.2153-3490.1959.tb00050.x

Twomey, S. (1991), Aerosols, clouds, and radiation, Atmos. Environ., 254, 2435–2442.

Várnai, T., and R. Davies (1999), Effects of Cloud Heterogeneities on Shortwave Radiation: Comparison of Cloud-Top Variability and Internal Heterogeneity, Journal of the Atmospheric Sciences, 56(24), 4206–4224, doi:10.1175/1520-0469(1999)056<4206:eochos>2.0.co;2.

Várnai, T., and A. Marshak (2007), View angle dependence of cloud optical thicknesses retrieved by Moderate Resolution Imaging Spectroradiometer (MODIS), Journal of Geophysical Research, 112(D6), doi:10.1029/2005jd006912.

Wood, R., C. R. Mechoso, C. S. Bretherton, R. A. Weller, B. J. Huebert, et al. (2011), The VAMOS Ocean-Cloud-Atmosphere-Land Study Regional Experiment (VOCALS-REx): goals, platforms, and field operations. Atmospheric Chemistry and Physics, European Geosciences Union, 2011, 11, pp.627-654. <10.5194/acp-11-627-2011>. <hal-00766427>

Wylie, D., E. Eloranta, J. D. Spinhirne, and S. P. Palm (2007), A Comparison of Cloud Cover Statistics from the GLAS Lidar with HIRS, Journal of Climate, 20(19), 4968–4981, doi:10.1175/jcli4269.1.

Zhang, M. H., et al. (2005), Comparing clouds and their seasonal variations in 10 atmospheric general circulation models with satellite measurements, J. Geophys. Res., 110, D15S02, doi:10.1029/2004JD0050

Zhang, Z., and S. Platnick (2011), An assessment of differences between cloud effective particle radius retrievals for marine water clouds from three MODIS spectral bands, Imaging and Applied Optics, doi:10.1364/hise.2011.htub3.

Zhang, Z., A. S. Ackerman, G. Feingold, S. Platnick, R. Pincus, and H. Xue (2012), Effects of cloud horizontal inhomogeneity and drizzle on remote sensing of cloud droplet effective radius: Case studies based on large-eddy simulations, Journal of Geophysical Research: Atmospheres, 117(D19), doi:10.1029/2012jd017655.

Zhang, Z. (2013), On the sensitivity of cloud effective radius retrieval based on spectral method to bi-modal droplet size distribution: A semi-analytical model, Journal of Quantitative

Spectroscopy and Radiative Transfer, 129, 79–88, doi:10.1016/j.jqsrt.2013.05.033.

Zhang, Z., F. Werner, H.-M. Cho, G. Wind, S. Platnick, A. S. Ackerman, L. D. Girolamo, A. Marshak, and K. Meyer (2016), A framework based on 2-D Taylor expansion for quantifying the impacts of subpixel reflectance variance and covariance on cloud optical thickness and effective radius retrievals based on the bispectral method, Journal of Geophysical Research: Atmospheres, 121(12), 7007–7025, doi:10.1002/2016jd024837.

Zinner, T., and B. Mayer (2006), Remote sensing of stratocumulus clouds: Uncertainties and biases due to inhomogeneity, J. Geophys. Res., 111, D14209, doi: 10.1029/2005JD006955.

Zinner, T., G. Wind, S. Platnick, and A.S. Ackerman (2010). Testing remote sensing on artificial observations: Impact of drizzle and 3-D cloud structure on effective radius retrievals. *Atmos. Chem. Phys.*, 10, 9535-9549, doi:10.5194/acp-10-9535-2010.

APPENDIX A: DATAFIELD LIST

Table A.1 Datafields in the Data Delivery for Texas A&M University

Product	Dataset Tree	SDS name
NIR BRF	NIR Band	NIR BRF
MIB2GEOP	GeometricParameters	SolarZenith
MIB2GEOP	GeometricParameters	SolarAzimuth
MIB2GEOP	GeometricParameters	DfZenith
MIB2GEOP	GeometricParameters	DfAzimuth
MIB2GEOP	GeometricParameters	CfZenith
MIB2GEOP	GeometricParameters	CfAzimuth
MIB2GEOP	GeometricParameters	BfZenith
MIB2GEOP	GeometricParameters	BfAzimuth
MIB2GEOP	GeometricParameters	AfZenith
MIB2GEOP	GeometricParameters	AfAzimuth
MIB2GEOP	GeometricParameters	AnZenith
MIB2GEOP	GeometricParameters	AnAzimuth
MIB2GEOP	GeometricParameters	AaZenith
MIB2GEOP	GeometricParameters	AaAzimuth
MIB2GEOP	GeometricParameters	BaZenith
MIB2GEOP	GeometricParameters	BaAzimuth
MIB2GEOP	GeometricParameters	CaZenith
MIB2GEOP	GeometricParameters	CaAzimuth
MIB2GEOP	GeometricParameters	DaZenith
MIB2GEOP	GeometricParameters	DaAzimuth
MOD06L2	mod06	Quality_Assurance_1km (Phase)
MOD06L2	mod06	Cloud_Optical_Thickness
MOD06L2	mod06	Cloud_Effective_Radius
MOD06L2	mod06	Cloud_Top_Pressure_1km
MOD06L2	mod06	Cloud_Top_Temperature_1km
MOD06L2	mod06	Cloud_Mask_SPI ($H\sigma$)
MOD06L2	mod06	Atm_Corr_Refl
MOD06L2	mod06	Cloud_Top_Height_1km
MIL2TCSP	Stereo_WithoutWindCorrection_1.1km	CloudTopHeight_WithoutWindCorrection